RESEARCH ARTICLE | JANUARY 20 2026

Emergence and dynamics of gas-accelerated liquid sheets: Insights into liquid chain formation

Krištof Kovačič ; Rizwan Zahoor ; Jernej Kušar ; Saša Bajt ; Božidar Šarler

Physics of Fluids 38, 012008 (2026)
https://doi.org/10.1063/5.0311193

Physics of Fluids ARTICLE pubs.aip.org/aip/pof

Emergence and dynamics of gas-accelerated liquid sheets: Insights into liquid chain formation

Cite as: Phys. Fluids **38**, 012008 (2026); doi: 10.1063/5.0311193
Submitted: 7 November 2025 · Accepted: 23 December 2025 ·
Published Online: 20 January 2026

View Online Export Citation CrossMark

Krištof Kovačič,[1] Rizwan Zahoor,[1] Jernej Kušar,[1] Saša Bajt,[2,3] and Božidar Šarler[1,a)]

AFFILIATIONS

[1]Laboratory for Fluid Dynamics and Thermodynamics, Faculty of Mechanical Engineering, University of Ljubljana, Aškerčeva 6, 1000 Ljubljana, Slovenia
[2]Center for Free-Electron Laser Science CFEL, Deutsches Elektronen-Synchrotron DESY, Notkestr. 85, 22607 Hamburg, Germany
[3]The Hamburg Centre for Ultrafast Imaging, Luruper Chaussee 149, 22761 Hamburg, Germany

[a)]Author to whom correspondence should be addressed: bozidar.sarler@fs.uni-lj.si

ABSTRACT

This study examines the behavior of liquid chain, open rim, and transitional jet–liquid chain regimes in gas-accelerated liquid micro-sheets using experimentally validated numerical simulations. The simulations employ the finite volume method with a volume-of-fluid framework to resolve compressible ideal gas flow impinging on a Newtonian, laminar liquid jet under atmospheric conditions. Adaptive mesh refinement is used to resolve the gas–liquid interface. The validation of the model is performed based on a purpose-built experimental setup over the range of gas–liquid momentum flux ratios $0.03 < \mathrm{MFR} < 2.6$, and Weber numbers, evaluated at the liquid capillary inlet, $3.8 < \mathrm{We} < 49$, achieving an agreement of the simulated liquid-sheet shape below experimental uncertainty. Three typical flow regimes are explained by the interplay of gas momentum, liquid inertia, and surface tension, scaled by the liquid-sheet rim Weber number ($\mathrm{We_{rim}}$), based on rim curvature and the rim transverse velocity. The transitional jet–liquid chain regime occurs at $\mathrm{We_{rim}} < 0.1$, where the surface tension dominates, resulting in only a slight change of the liquid jet cross section. In the liquid chain regime ($0.1 < \mathrm{We_{rim}} < 1$) gas inertia forms the sheet, then surface tension bends the rim inward, and transverse momentum transfer forms an orthogonal secondary link. In the open rim regime ($\mathrm{We_{rim}} > 2$), dominant rim inertia prevents sheet closure. The Weber number (We), based on the nozzle inlet parameters, can predict the liquid chain regime in the range $1.5 \lesssim \mathrm{MFR\,We}^{0.84} \lesssim 4$. This relation provides practical guidance for stable liquid chain operation.

I. INTRODUCTION

In recent years, liquid sheets and chains, capable of forming stable, continuous, and flat jets with submicrometer thickness, have emerged as promising candidates for sample delivery systems in serial femtosecond crystallography (SFX)[1] and other probing measurements.[2–4] In SFX, femtosecond x-ray pulses, produced by an x-ray free-electron laser (XFEL), are used to diffract of protein microcrystals delivered into the x-ray beam via liquid jets. Intense XFEL pulses are required to get measurable Bragg diffraction of such small and weakly scattering samples. During this process, the samples are destroyed. However, since the pulses are also extremely short (femtoseconds), the diffraction patterns can be recorded before destruction ("diffraction-before-destruction"[1]). Hence, a continuous supply of microcrystals must be delivered and removed from the X-ray interaction region. Over the years, various sample delivery systems have been developed,[5] but most recently, liquid sheets have emerged as a new promising approach. Unlike cylindrical microjets,[6,7] whose curved geometry and droplet breakup complicate beam alignment and increase background scattering,[8] flat liquid sheets offer a large, well-defined interaction area that is well suited for experiments with limited beam focusing, such as ultrafast electron diffraction (UED).[3] For example, sub micrometer sheet-jet thickness was achieved with different nozzle designs, including two oblique colliding liquid jets,[9–21] a converging nozzle[22–24] and focusing a liquid jet with two liquids[25] or gas[3,12,16,24,26,27] oblique capillaries, transforming a cylindrical jet into a liquid chain, a series of consecutive, orthogonal sheet links. The final design in this list, known as the gas-accelerated liquid-sheet nozzle,[27] resulted in the thinnest flat sheet jets so far. In a liquid sheet, with a uniform thickness over a large area, often expressed as optical flatness, background signal fluctuations are reduced. At the same time, the small liquid-sheet thickness enables x-ray scattering and spectroscopic investigations, approaching the single-molecule scale.[27]

The liquid sheet, a thin flat jet, bounded by a curved rim, was first demonstrated by Savart.[28] The physics of liquid sheets produced by two impinging liquid jets has been studied extensively since the pioneering works of Dombrowski[29] and Taylor.[30] Dombrowski and Fraser[29] systematically investigated the different flow regimes of flat jets, produced by various types of apparatus, classified according to the manner in which the energy is imparted to the liquid. They also examined the influence of liquid properties and air friction, demonstrating that aerodynamic shear induces instabilities that promote the disintegration of the sheet. Taylor[30] focused on flat sheets formed by obliquely impinging jets, analyzing their geometry and thickness and identifying the key balance between inertia and surface tension that governs sheet stability. He also derived the first model for predicting the sheet thickness. In the following decades, several scaling laws were proposed to improve the prediction of sheet thickness.[31–35]

Under certain flow conditions, a liquid sheet forms a sequence of consecutive, orthogonally oriented sheet segments bounded by curved rims, a configuration referred to as the fluid chain or liquid chain regime. This regime has been reported previously[29,36] but not examined in detail. Bush and Hasha[37] performed the first systematic investigation of liquid chains, demonstrating that their dynamics are primarily governed by the interplay between fluid inertia and surface tension, which produces stable, periodic, chain-like structures. Their experiments revealed that fluid viscosity plays a crucial stabilizing role by regulating rim size and suppressing capillary instabilities that would otherwise lead to sheet breakup. Consequently, the fluid chain regime emerges within a finite range of Reynolds and Weber numbers, delineating the transition between oscillating streams, open rim, fishbones, spluttering chains, disintegrating sheets and violent flapping regimes.[37]

In this paper, we are particularly interested in liquid sheets produced by two oblique gas streams impinging on a central liquid jet.[26] The introduction of external gas flow around the liquid jet adds an additional layer of complexity to the physical mechanisms governing sheet-jet dynamics and the emergence of distinct flow regimes. Gas-accelerated liquid sheets have been demonstrated experimentally, and their characteristic parameters, such as sheet length, width, and the thickness of the primary link, have been measured.[3,4,16,24,26,27] However, the underlying physical mechanisms are still not fully understood.

Numerical simulations of flat sheet jets[38] can provide details that are difficult to measure experimentally. These simulations have informed nozzle design optimization[39,40] and provide a deeper understanding of the physics behind the interaction of focusing gas and liquid jet.[41–47] Here, we perform the first experimentally validated numerical model to investigate the dynamics of gas-accelerated flat sheet jets, which was missing in our earlier study.[38] We also use a more realistic nozzle design with a 30 μm capillary diameter, suitable for SFX experiments and avoiding clogging issues associated with the 20 μm nozzle used previously. In addition to the earlier study, which focused only on the liquid chain regime, the simulations in this study aim to elucidate the physical mechanisms underlying the formation of liquid chain, open rim, and transitional jet–liquid chain regimes and identify the governing dimensionless parameters by clarifying the coupled roles of gas momentum, liquid inertia, and surface tension in determining the observed flow regimes.

The investigated parameter space spans $76 < \mathrm{Re_g} < 332$, $91 < \mathrm{Re_l} < 336$, $3.8 < \mathrm{We} < 49$, and $0.04 < \mathrm{Ca} < 0.15$, where $\mathrm{Re_g} = \rho_g v_g D_g/\mu_g$ and $\mathrm{Re_l} = \rho_l v_l D_l/\mu_l$ are the gas and liquid Reynolds numbers, $\mathrm{We} = \rho_l v_l^2 D/\sigma$ is the Weber number, and $\mathrm{Ca} = \mu_l v_l/\sigma$ is the capillary number. Here, ρ, μ, σ, v, and D denote density, dynamic viscosity, surface tension, characteristic velocity, and the diameter of the nozzle's feeding capillary, respectively. These ranges of nondimensional numbers provide an in-depth view of the physical behavior, advancing the understanding of the physics of gas-accelerated sheet jets.

The present work extends the state-of-the-art impinging jet simulations,[48] incorporating a compressible helium flow that actively focuses and accelerates the liquid jet into a sheet. In contrast, earlier studies considered the surrounding gas only as a quiescent medium, without modeling high-velocity compressible flow. This configuration introduces significant numerical challenges due to the large velocity ($v_g/v_l \sim 40{:}1$) and density ($\rho_g/\rho_l \sim 1{:}5000$) ratios between phases, requiring time steps on the order of 10^{-9}–10^{-10} s to ensure stability. Beyond validation, we introduce the rim Weber number $\mathrm{We_{rim}} = \rho_l v_{l,y,rim}^2 R_{rim}/\sigma$ as a local parameter governing sheet closure and demonstrate how the balance of transverse inertia ($\rho_l v_{l,y,rim}^2 R_{rim}$) and surface tension ($\sigma$) explain the emergence of different regimes. While previous studies[49] typically evaluated the global sheet Weber number using the central sheet thickness and velocity, this study focuses on the rim region, where inertia and surface tension directly govern the sheet dynamics. This is analogous to rim Weber numbers used in droplet dynamics to characterize rim or ligament breakup.[50–52] Furthermore, we demonstrate that the liquid chain regime can be predicted from nozzle geometry and flow rates alone through a power-law relation between the momentum flux ratio, $\mathrm{MFR} = \rho_g v_{g,x}^2/\rho_l v_{l,z}^2$ and Weber number We, providing a practical criterion for experimental operation.

In Sec. II, we present the experimental setup, measurements, and their associated uncertainty. Section III describes the governing equations, spatial discretization, boundary and initial conditions, and solver settings, followed by a grid convergence study. Section IV contains the main results and discussion. It includes temporal and spatial analyses of the primary sheet link dimensions, as well as experimental validation and visualization of flow and recirculation zones. It also presents the introduction of $\mathrm{We_{rim}}$ as a local closure criterion and the proposed predictive scaling law that delineates the liquid chain regime from open rim and transitional cases. The section concludes with a comparison of width, length, and thickness across all cases. The final section summarizes the key findings.

II. EXPERIMENT

A. Experimental setup

The purpose-built experimental setup was designed to validate the numerical simulations by comparing the liquid-sheet regimes, widths, and lengths. The experimental setup closely follows previous studies,[53–55] with two key differences: it was conducted under atmospheric conditions (no vacuum chamber) and it was specifically designed to allow a systematic evaluation of experimental uncertainty, enabling precise and reproducible measurements of sheet widths and lengths (see Sec. II C for details).

The nozzle used in experiments, designed to generate gas-accelerated flat sheet jets, was fabricated using a Nanoscribe Photonic Professional GT two-photon polymerization (2PP) printer with general-purpose resin (IP-S), achieving a precision of 0.2 μm.[56] The printing for a single nozzle took 2 h, followed by an 8 h development

procedure. The same nozzle design was printed three times to verify the reproducibility of liquid-sheet operation. A detailed description of the nozzle fabrication can be found in Ref. 53.

A schematic representation of the setup is provided in Fig. 1. The gas-accelerated liquid-sheet nozzle (A) was mounted on a piezoelectrically actuated stage, enabling precise translation in three directions and rotation around one axis. A syringe pump (Nemesys) (B) provided the volumetric flow of the de-ionized water. The helium flow was supplied from a pressurized tank. The gas mass flow meter (Bronkhorst F-111B-200) (C) measured the helium flow, which was set by a pressure regulator (D). The liquid sheet was illuminated by the system (E), which utilized a laser-induced fluorescence (iLIF) with a dual-pulse laser system [Litron Nano S 50–20 particle image velocimetry (PIV) Nd:YAG laser (532 nm)]. However, the laser only generated a single pulse, providing sufficiently bright illumination. A coherent laser beam was directed through an optical path into a cuvette containing a rhodamine 6 G suspension, which absorbed the laser light and re-emitted at 568 nm, providing spatially incoherent illumination of the liquid sheet. A sCMOS camera (Andor Zyla 5.5) (G) captured the liquid-sheet dynamics for visualization. The camera was equipped with a long-working-distance objective (LMPLFLN 20×, Olympus) (F), facilitating detailed imaging of the primary liquid-sheet formation. The camera was triggered by an external digital delay generator (DG635/15, Stanford Research Systems) (H) to ensure synchronization with the pulsed illumination. The exposure time of the sCMOS camera was set to 66.67 μs to match the laser pulse, which provided optimal illumination of the sheet. Under these conditions, the camera operated at 15 fps. This frame rate is sufficient for distinguishing the observed flow regimes, particularly the steady liquid chain regime, and therefore, no high-speed camera was required.

B. Experimental measurements

The images of the liquid sheets were captured for a given combination of helium mass flow rate $\dot{m}_g$ and de-ionized water volumetric flow rate Q_l. Images were analyzed in ImageJ software. Due to the grainy background and the subsequently challenging automatic analysis, the maximum width (W) of the primary liquid sheet and its length (L) were manually measured 20 times for each of the three printed nozzles of the same nozzle design at a given $\dot{m}_g$ and Q_l combination.

To determine the end of the primary sheet, we identified the position where the two rims converge along the jet axis. In the raw images, this convergence region appears relatively dark because the surface becomes smoother, which reduces specular reflection toward the camera. Immediately downstream, where the secondary sheet forms, the image intensity increases sharply. This occurs because the upper rim of the secondary sheet is strongly curved and oriented in a way that it reflects more light into the camera, producing a noticeably brighter region. We therefore defined the sheet end as the location where the pixel intensity changes abruptly from the darker convergence zone to the brighter region associated with the secondary sheet.

To convert pixels to micrometers, we performed a camera calibration, where we measured the distance of a reference object of a known distance L_{ref}. In our case, a nozzle width (52 μm) was used as a reference distance P_{ref}. The liquid-sheet length L was converted from pixels to micrometers with a simple equation

$$L = L_{px}\, C = L_{px} \frac{L_{ref}}{P_{ref}}, \tag{1}$$

where L_{px} is the length in pixels measured on the image and C is a calibration constant, defined by the ratio between the distance of the reference object L_{ref} (μm) and its measured distance in the image P_{ref} (px). The maximum width of the primary liquid sheet is measured in the same way. Figure 2 illustrates the width and the length of the primary liquid sheet.

C. Measurement uncertainty

Measurement uncertainty is evaluated according to the JCGM 100:2008 standard.[57] The procedure for measuring the length and the width of the sheet consists of three parts: image processing, calibration, and measurement of its width and length. Each of these parts contributes to the final, combined uncertainty. The sources of the uncertainty during the image processing are the distortion of the camera (reprojection error) u_{reproj}, binarization u_{bin}, and camera resolution u_{res}, which contribute to the uncertainty when measuring the distance in pixels $u(P_{ref})$. In the calibration step, the printer resolution affects the uncertainty of the nozzle dimensions $u(L_{ref})$. Finally, the standard uncertainty of the length measurements combines all previous uncertainties, which are demonstrated schematically in Fig. 3.

For our measurements, we evaluated expanded uncertainty with a coverage factor $k = 2$, corresponding to ~95% confidence.[57] The expanded uncertainty is a product of the coverage factor and standard uncertainty $U(L) = k\, u(L)$. The measured averaged liquid sheet width and length from all three printed nozzles (20 measurements per nozzle) are $49.20 \pm 3.29\,\mu$m and $214.60 \pm 14.35\,\mu$m, respectively. The expanded uncertainty of both dimensions is ~7% of their average value, demonstrating nozzle's reproducibility. Further information on uncertainty determination can be found in Appendix A.

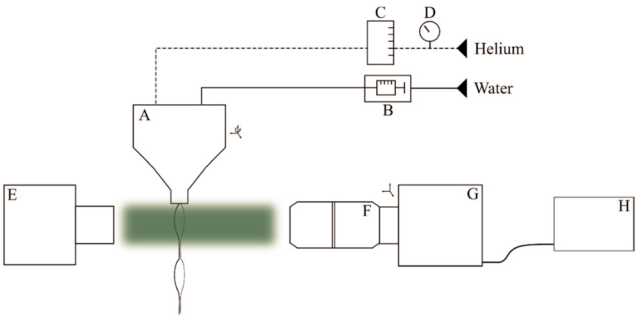

FIG. 1. Experimental setup: (A) gas-accelerated liquid-sheet nozzle, (B) syringe pump, (C) gas mass flow meter, (D) pressure regulator, (E) illumination system, (F) objective, (G) sCMOS camera, and (H) digital delay generator.

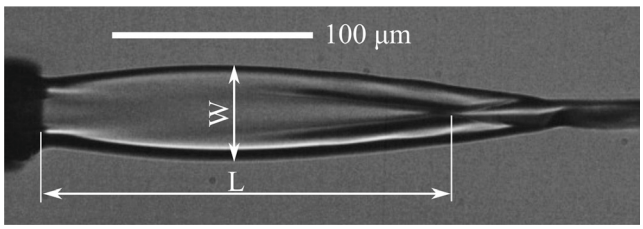

FIG. 2. Width and length determination of the primary liquid sheet from the experimental frame. Flow rates: helium 12.6 mg min^{-1}, water 600 μl min^{-1}.

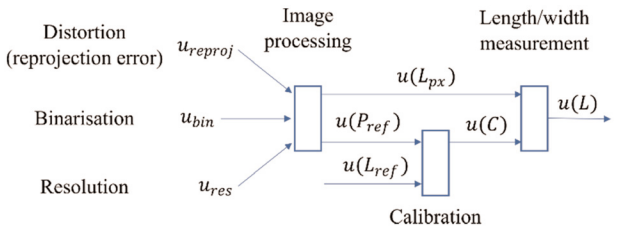

FIG. 3. Scheme of the evaluation of the flat sheet jet's width and length uncertainty.

III. NUMERICAL FORMULATION

A. Governing equations

The analysis of two-phase, Newtonian, unsteady, and laminar compressible gas (helium) and incompressible Newtonian liquid (water) flow is solved in ANSYS Fluent 2024R1 release,[58] which is based on the finite volume method (FVM). The liquid–gas interface is calculated using the explicit volume-of-fluid (VOF) method with the piecewise linear interface calculation (PLIC), known as the geometric reconstruction scheme. In VOF, a volume fraction $\alpha(\boldsymbol{p}, t)$, which is a function of the position $\boldsymbol{p}(x, y, z)$ and time t, determines the phases

$$\alpha(\boldsymbol{p}, t) = \begin{cases} 1 & \boldsymbol{p} \text{ in liquid,} \\ 0 & \boldsymbol{p} \text{ in gas.} \end{cases} \tag{2}$$

The gas–liquid interphase boundary is calculated by an advection equation with a discontinuity in α at the interphase boundary

$$\frac{\partial}{\partial t}(\rho\,\alpha) + \nabla \cdot (\rho\,\boldsymbol{v}\,\alpha) = 0, \tag{3}$$

where $\boldsymbol{v}(\boldsymbol{p}, t)$ is the velocity vector and ρ is density, which is, along with the other material properties, such as dynamic viscosity μ, specific heat c_p, and thermal conductivity k, determined by the phase-weighted average

$$\vartheta(\alpha) = \alpha\vartheta_l + (1-\alpha)\vartheta_g, \tag{4}$$

where ϑ_l and ϑ_g stand for liquid and gas properties, respectively.

The governing equations of mass, momentum, and energy conservation, posed in mixture formulation, are the following:

$$\frac{\partial \rho}{\partial t} + \nabla \cdot (\rho \boldsymbol{v}) = 0, \tag{5}$$

$$\frac{\partial}{\partial t}(\rho \boldsymbol{v}) + \nabla \cdot (\rho \boldsymbol{v}\boldsymbol{v}) = -\nabla P + \nabla \cdot \bar{\boldsymbol{\tau}} + \sigma\kappa\nabla\alpha, \tag{6}$$

$$\frac{\partial}{\partial t}(\rho e) + \nabla \cdot (\rho \boldsymbol{v} e) = -\nabla \cdot (P\boldsymbol{v}) + \nabla \cdot (k\nabla T) + \nabla \cdot (\bar{\boldsymbol{\tau}}\,\boldsymbol{v}), \tag{7}$$

where $P(\boldsymbol{p}, t)$ denotes pressure and $\bar{\boldsymbol{\tau}}$ viscous stress tensor, defined as $\bar{\boldsymbol{\tau}} = \mu\left[(\nabla \boldsymbol{v}) + (\nabla \boldsymbol{v})^T\right] - 2/3\,\mu(\nabla \cdot \boldsymbol{v})\mathbf{I}$, where μ and $\mathbf{I}$ stand for dynamic viscosity and identity tensor, respectively. For the analyzed helium flow, bulk viscosity is not included because monatomic gases exhibit negligible bulk viscosity.[59–69] The term $\sigma\kappa\nabla\alpha$ in Eq. (6) represents the surface tension force, which is defined by a surface tension σ, curvature κ, calculated by the continuum surface model (CSF) $\kappa(\alpha) = -\nabla \cdot \left(\nabla\alpha/|\nabla\alpha|\right)$, and the gradient of a volume fraction $\nabla\alpha$. In Eq. (7), T stands for the temperature and e for total specific energy $e = c_p T - P/\rho + 0.5|\boldsymbol{v}|^2$. The terms on the right-hand side of Eq. (7) represent work done by pressure forces, the Fourier heat flux, and viscous dissipation, respectively. The ideal gas law expresses the gas density

$$\rho_g = \frac{PM}{RT}, \tag{8}$$

where R and M are the universal gas constant and molar mass, respectively. The dynamic viscosity of the gas is treated as being temperature dependent, and it is determined from the Sutherland law

$$\mu_g = \frac{A_S\sqrt{T}}{1 + \frac{T_S}{T}}, \tag{9}$$

with values for helium $A_S = 1.48 \times 10^{-6}\,\mathrm{kg\,m^{-1}\,s^{-1}K^{-1/2}}$ and $T_S = 79\,\mathrm{K}$.[70]

B. Computational domain and setup

The nozzle design is shown in Fig. 4(a). The computational fluid domain was extracted from the bottom part of the nozzle. The cross section of the fluid domain is shown in Fig. 4(b). Due to the symmetrical nozzle design, only a quarter of the nozzle geometry needs to be calculated, resulting in a significant reduction in computational time. Figure 4(c) shows the discretized fluid domain, consisting of hexahedral elements. These elements are ordered hierarchically based on the octree concept. A cell size h is defined by its hierarchical level l with $h_l = 1.6\,D/2^l$, where D is the diameter of the liquid (gas) capillary (30 μm). A cell at level l is a parent to eight child cells at level $l+1$. All cells at levels $l > 0$ are based on the root cell at the zeroth level $l = 0$. The computational mesh comprises six static levels ($l \in [0,5]$), while additional levels are adaptive. Three different computational grids were tested to perform a mesh independence study. The finest mesh M1 has three additional levels (min. cell size $h_8 = 188\,\mathrm{nm}$), while the coarsest mesh M3 has only one additional adaptive level (min. cell size $h_6 = 750\,\mathrm{nm}$). Figure 4(d) shows the detail of the mesh M2 (min. cell size $h_7 = 375\,\mathrm{nm}$) at the nozzle outlet. The adaptive mesh refinement (AMR) algorithm refines the gas–liquid interface with additional refinement levels ($l > 5$) based on the gradient of the volume fraction. The global maximum scales the values of the gradient of the volume fraction. Cells with a gradient value higher than 0.06 are refined, whereas those with a gradient value lower than 0.05 are coarsened. AMR is performed every 20 time steps and utilizes four additional refinement layers of the finest AMR level, providing a refined interface and a high-resolution mesh near the interface.

The computational domain comprises five types of boundaries: gas mass flow inlet (A), liquid mass flow inlet (B), symmetry (C), no-slip walls (D), and pressure outlet (E), as illustrated in Fig. 4(c) and summarized in Table I. To improve numerical stability, an initial gauge pressure P_i is applied at the helium inlet. For each distinct gas flow, P_i was obtained from separate single-phase helium simulations through the nozzle, similar to Ref. 71. The resulting velocity, pressure, temperature, and density fields were then used as initial conditions for the transient two-phase flow simulation, reducing computation time and improving numerical stability. Similarly, the liquid capillary was initialized with velocity, pressure, temperature, and density fields of water and patched with a water volume fraction at the start of the simulation.

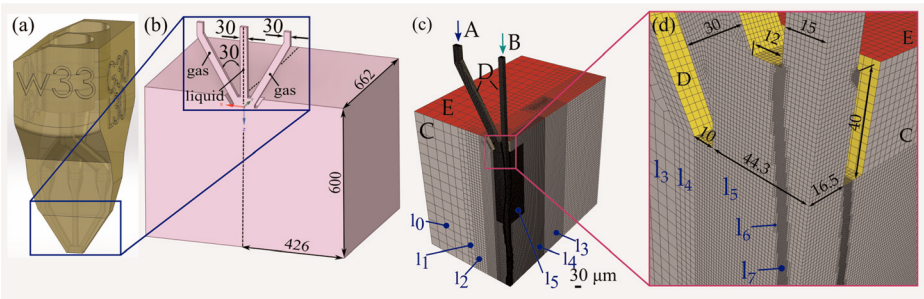

FIG. 4. Nozzle model, fluid domain, and computational grid: (a) actual gas-accelerated liquid flat sheet-jet nozzle, (b) extracted computational domain, (c) discretized 1/4 of the fluid domain (mesh M2), and (d) detail of the mesh M2 around the nozzle outlet. Boundary conditions: A—gas mass flow inlet (blue), B—liquid mass flow inlet (cyan), C—symmetry (gray), D—no-slip walls (yellow), E—pressure outlet (red). All dimensions are expressed in μm and degrees.

TABLE I. Boundary conditions.

Mark	Type	Mass flow/velocity	Pressure	Temperature	Phase fraction
A	Gas inlet	$1/4\,\dot{m}_g$	P_i	$T = 293\,\mathrm{K}$	$\alpha = 0$
B	Liquid inlet	$1/4\,Q_l\,\rho_l$	$\partial P/\partial \boldsymbol{n} = 0\ \mathrm{Pa\ m^{-1}}$	$T = 293\,\mathrm{K}$	$\alpha = 1$
C	Symmetry	$\partial \boldsymbol{v}/\partial \boldsymbol{n} = 0\ \mathrm{s^{-1}}$	$\partial P/\partial \boldsymbol{n} = 0\ \mathrm{Pa\ m^{-1}}$	$\partial T/\partial \boldsymbol{n} = 0\ \mathrm{K\ m^{-1}}$	$\partial \alpha/\partial \boldsymbol{n} = 0\ \mathrm{m^{-1}}$
D	Walls	$\boldsymbol{v} = 0\ \mathrm{m\,s^{-1}}$	$\nabla P \cdot \boldsymbol{n}$[a]	$T = 293\,\mathrm{K}$	$\theta_{contact} = 90°$
E	Outlet	$\partial \boldsymbol{v}/\partial \boldsymbol{n} = 0\ \mathrm{s^{-1}}$	$P = 101\,325\,\mathrm{Pa}$	$\partial T/\partial \boldsymbol{n} = 0\ \mathrm{K\ m^{-1}}$	$\partial \alpha/\partial \boldsymbol{n} = 0\ \mathrm{m^{-1}}$

[a]The pressure is calculated from the momentum and continuity equations.

Velocity profiles, defined through mass flow rates, at both inlets are uniform. Therefore, the model includes a sufficiently long upstream section of the nozzle to ensure fully developed velocity profiles near the gas and liquid capillary outlet. Symmetry boundary conditions were applied along two planes, reducing the computational domain to a quarter of the nozzle geometry.

The system of equations described above is solved on the high-performance computing (HPC) cluster (AMD EPYC 7402, 2.8 GHz) using two nodes with 48 cores each.

The pressure–velocity coupling of the pressure-based solver is performed with the coupled scheme, which provides the most stable numerical simulation. The gradients are discretized using a least squares cell-based approach and pressure is handled with the PRESTO! method. The density, momentum, and energy equations are discretized with the second-order upwind (SOU) scheme. The transient formulation is described using a first-order implicit scheme with an adaptive time step. The time step size is determined through the Courant–Friedrichs–Lewy (CFL) condition, defined as $\mathrm{CFL} = u\,\Delta t/\Delta x$, where u is the velocity in the computational cell, Δt is the time step size, and Δx is the minimal edge length of the cell. The maximum allowed CFL number is $\mathrm{CFL}_{max} = 0.75$. Consequently, the typical time step sizes for the different meshes are 0.95 ns for the fine mesh M1 ($\Delta x = h_8 = 188\,\mathrm{nm}$), 1.15 ns for the medium mesh M2 ($\Delta x = h_7 = 375\,\mathrm{nm}$), and 1.30 ns for the coarse mesh M3 ($\Delta x = h_6 = 750\,\mathrm{nm}$). The transient formulation of the VOF equation is calculated with the explicit scheme, where the local CFL is limited to 0.25. Convergence criteria are set to 10^{-4} for the continuity equation and 10^{-6} for momentum and energy equations, which are typically reached on average within three to five iterations per time step.

C. Grid convergence

A grid convergence study (GCS) has been performed on meshes M1, M2, and M3, which contain 10×10^6, 1.8×10^6, and 0.85×10^6 cells, respectively. The time-averaged width W, length L, and thickness H of primary liquid sheet, evaluated after the primary sheet reaches a stabilized (steady-state) shape, are chosen as an integral representative variable Φ for GCS, which is performed by a well-known approach[72,73] with a representative grid size, defined as

$$h = \left[\frac{1}{N}\sum_{i=1}^{N}(\Delta V_i)\right]^{1/3}, \tag{10}$$

where N is the total number of cells and ΔV_i is the volume of i th cell. Meshes M1–M3 have been constructed considering the grid refinement factor $r = h_3/h_1$ larger than 1.3, as recommended by Roache.[72,73] For meshes where $r_{21} = h_2/h_1$ and $r_{32} = h_3/h_2$ are not constant ($r_{21} \neq r_{32}$), the order of convergence p is defined using the following equations:

$$p = \frac{\left|\ln\left|\frac{\epsilon_{32}}{\epsilon_{21}}\right| + q(p)\right|}{ln(r_{21})}, \tag{11}$$

$$q(p) = \ln\left(\frac{r_{21}^{p} - s}{r_{32}^{p} - s}\right), \tag{12}$$

$$s = \frac{\epsilon_{32}/\epsilon_{21}}{|\epsilon_{32}/\epsilon_{21}|}, \tag{13}$$

where $\epsilon_{32} = \Phi_3 - \Phi_2$, $\epsilon_{21} = \Phi_2 - \Phi_1$ and Φ_k denote the solution of the chosen representative variable on the k th grid. Equations (11) and (12) should be solved iteratively. If $r_{21} = r_{32} = \mathrm{const}$, then $q(p) = 0$, and thus, there is no need for iterative calculations. The extrapolated value Φ_{ext}^{21} is calculated as

$$\Phi_{ext}^{21} = \frac{r_{21}^{p}\Phi_1 - \Phi_2}{r_{21}^{p} - 1}. \tag{14}$$

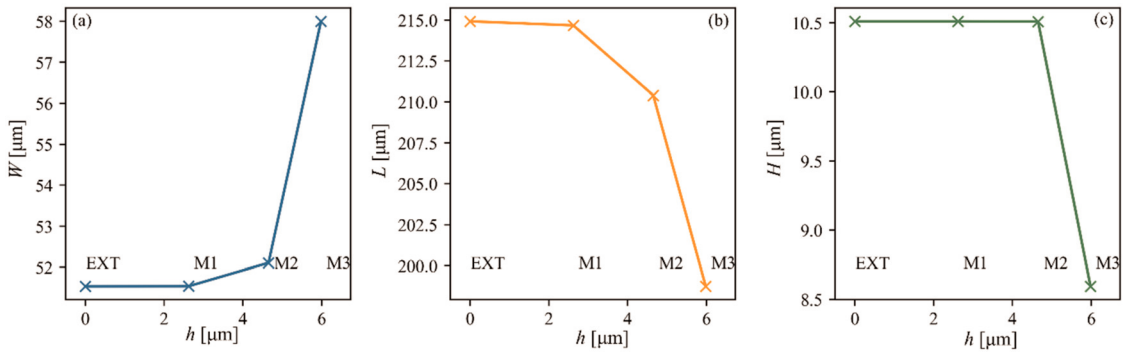

FIG. 5. Grid convergence study: (a) primary width of the sheet vs representative grid size, (b) primary length of the sheet vs representative grid size, and (c) primary thickness of the sheet vs representative grid size. M1–M3 indicate the values calculated with three different meshes. EXT indicates extrapolated value.

TABLE II. Grid convergence study for representative variable Φ in terms of liquid-sheet width, length and thickness.

Variable	r_{21}	r_{32}	$\Phi_1(\mu m)$	$\Phi_2(\mu m)$	$\Phi_3(\mu m)$	p	$\Phi_{ext}^{21} * (\mu m)$	$e_a^{21}(\%)$	$e_{ext}^{21}(\%)$	$GCI^{32}(\%)$	$GCI^{21}(\%)$
Width	1.77	1.29	51.54	52.11	58.00	9.66	51.54	1.10	0.00	1.51	0.01
Length	1.77	1.29	214.67	210.40	198.75	5.06	214.92	1.99	0.12	3.46	0.14
Thickness	1.77	1.29	10.512	10.510	8.595	27.71	10.512	0.02	0.00	0.02	0.00

Φ_{ext}^{32} is calculated analogously. Two different errors are analyzed: approximate relative error e_a^{21} and extrapolated relative error e_{ext}^{21}, respectively,

$$e_a^{21} = \left|\frac{\Phi_1 - \Phi_2}{\Phi_1}\right|, \tag{15}$$

$$e_{ext}^{21} = \left|\frac{\Phi_{ext}^{21} - \Phi_1}{\Phi_{ext}^{21}}\right|. \tag{16}$$

Finally, the grid convergence index (for fine mesh M1) is defined as follows:

$$GCI^{21} = \frac{F_S\, e_a^{21}}{r_{21}^p - 1}, \tag{17}$$

where the security factor F_S equals 1.25 for three meshes or more, as suggested by Roache.[72] GCI^{32} and e_a^{32} are calculated analogously.

Figures 5(a)–5(c) illustrate the grid convergence for the width W, length L, and thickness H of the primary sheet, respectively. The GCI^{21} for all dimensions of the sheets is close to zero (rounded to two decimal places). Low GCI^{21} shows that the results for meshes M2 and onward are mesh independent. Thus, the M2 mesh is chosen for further numerical investigation. The solution at the same time step for all three meshes is illustrated in Fig. 6. Table II presents the results for GCS. To calculate a physically realistic behavior, a minimum of three computational nonadaptive cells (min. size 1.5 μm) across the radius of the thinnest section ($\sim$5 μm) of the sheet jet is required, supplemented by at least two AMR levels of the interface—a criterion satisfied by M1 and M2 but not by M3 mesh.

IV. RESULTS AND DISCUSSION

We investigated 25 distinct combinations of water and helium flow rates, as shown in Fig. 7(a), where a representative of each observed regime type is illustrated in Figs. 7(b)–7(e). Numerical simulations correctly reproduce the experimentally observed flow regimes: (b) the liquid chain, (e) the open rim, and two transitional regimes (c) from the cylindrical jet to liquid chain, and (d) from the liquid chain to open rim.

The numerical simulations for each regime were calculated until the initial transient period of liquid-sheet formation had passed and its shape had stabilized. Figure 8 presents the evolution of the maximum width (a) and minimum thickness (b) of the primary link in the liquid chain for the flow combination of 12.6 mg min^{-1} helium and 600 μl min^{-1} water, with the sheet thickness stabilizing after 36 μs and the width after 40 μs (multimedia available online).

Once the stabilized solution was reached, the sheet characteristics, including length L, width W, and thickness H, were extracted over stabilized time intervals by tracking its cross-sectional shape, as shown in

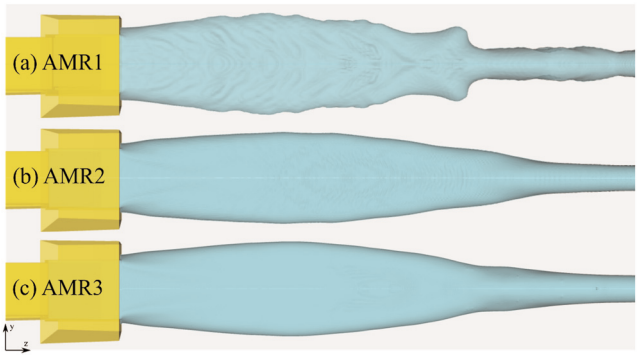

FIG. 6. Results with different levels of AMR at 56.15 μs (after the sheet shape is stabilized): (a) M3 with one level of AMR, (b) M2 with two levels of AMR, and (c) M1 with three levels of AMR.

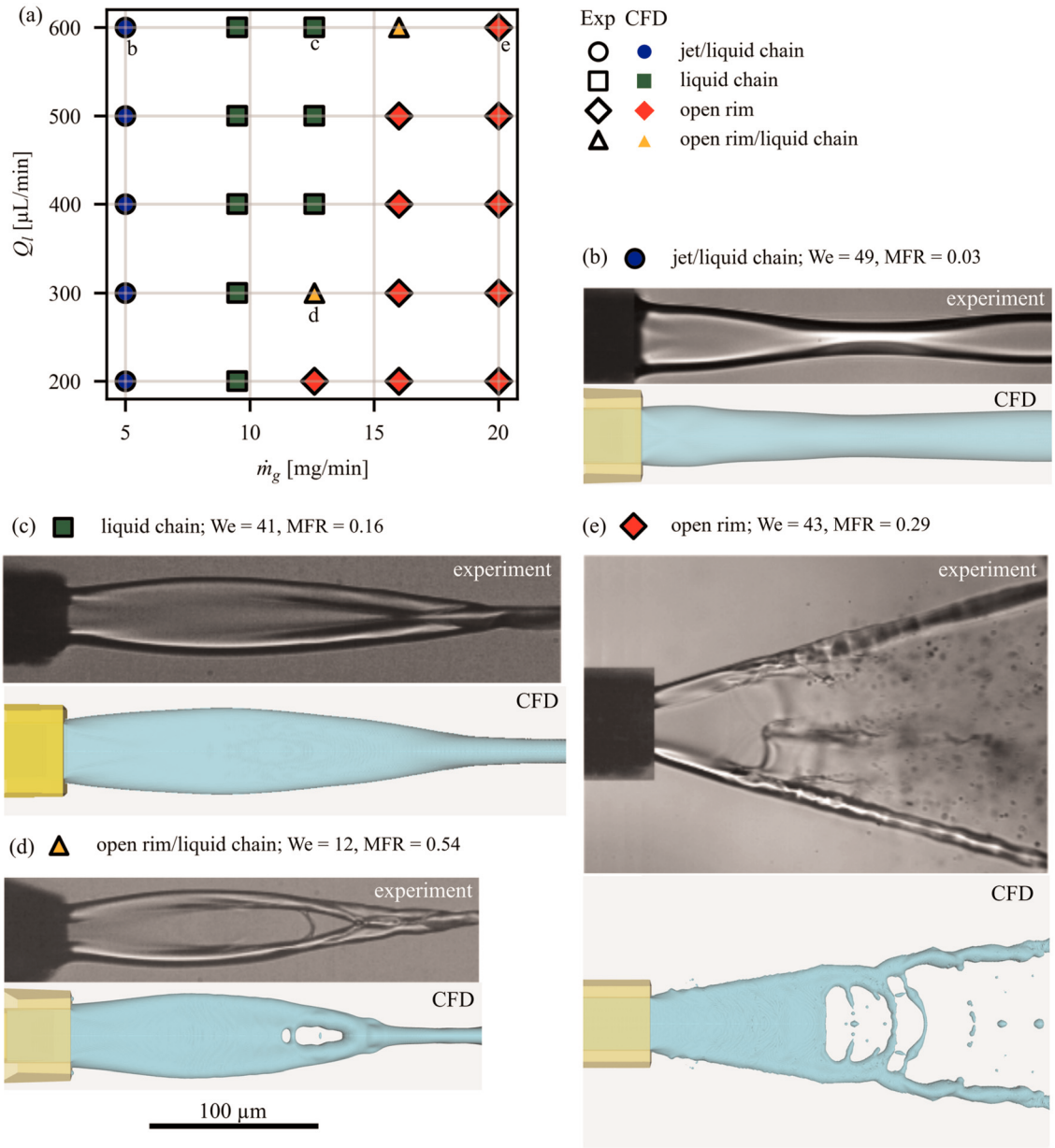

FIG. 7. Flow pattern map (a) for analyzed cases. Panels (b)–(e) compare experimental and numerical results for representative flow regimes: (b) transitional jet–liquid chain regime, $W = 38.7\ \mu m$, $L = 86.3\ \mu m$, $H = 24.4\ \mu m$; (c) liquid chain, $W = 52.1\ \mu m$, $L = 210.4\ \mu m$, $H = 10.5\ \mu m$; (d) open rim–liquid chain transition, $W = 54.7\ \mu m$, $L = 177.9\ \mu m$, $H = 2.0\ \mu m$; and (e) open rim, $W = 68.7\ \mu m$, $L = 154.2\ \mu m$, $H = 1.65\ \mu m$. For the analyzed flow rate combination, the numerical and experimental results exhibit the same flow pattern.

Fig. 9. The primary, secondary, and tertiary sheet link cross sections are shown in Fig. 9. The sheet width and thickness are measured between interface boundaries ($\alpha = 0.5$), and link transitions are identified when the aspect ratio along the sheet axis approaches $W/H \approx 1$, corresponding to a near-circular cross section. The transitions between consecutive sheet links can be clearly seen through W/H ratio along the sheet axis in Fig. 10(a).

The primary link is the widest and the thinnest, while subsequent links become progressively narrower and thicker, consistent with the width and thickness trends along the jet [see Figs. 10(b) and 10(c)]. The thickness decreases until the formation of the subsequent link, with minimum values along the nozzle axis occurring at 57%, 42%, and 45% of the length of the first, second, and third orthogonal links, respectively.

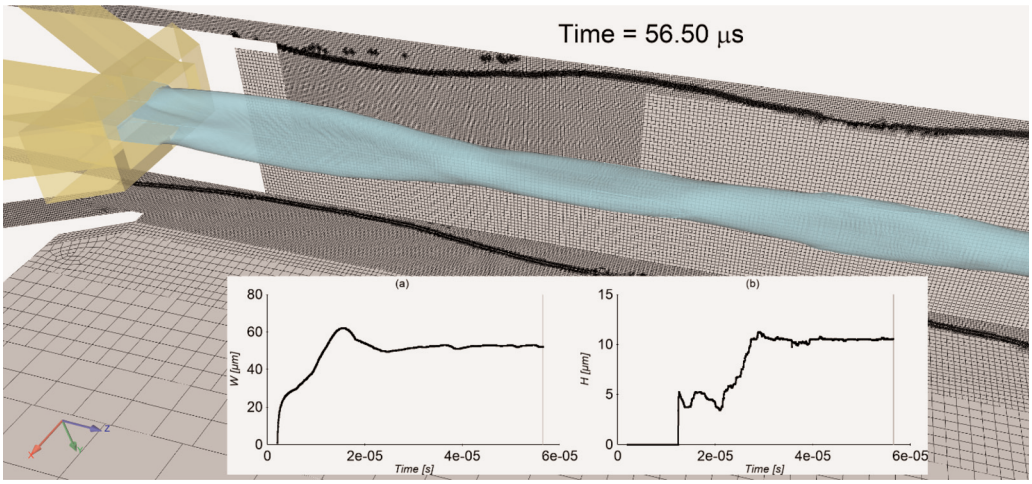

FIG. 8. Temporal evolution of the maximum width (a) and the minimum thickness (b) of the primary sheet link. The sheet-jet evolution for helium (12.6 mg min^{-1}) and water (600 μl min^{-1}) flow is shown along with AMR cells on both symmetry planes. Multimedia available online.

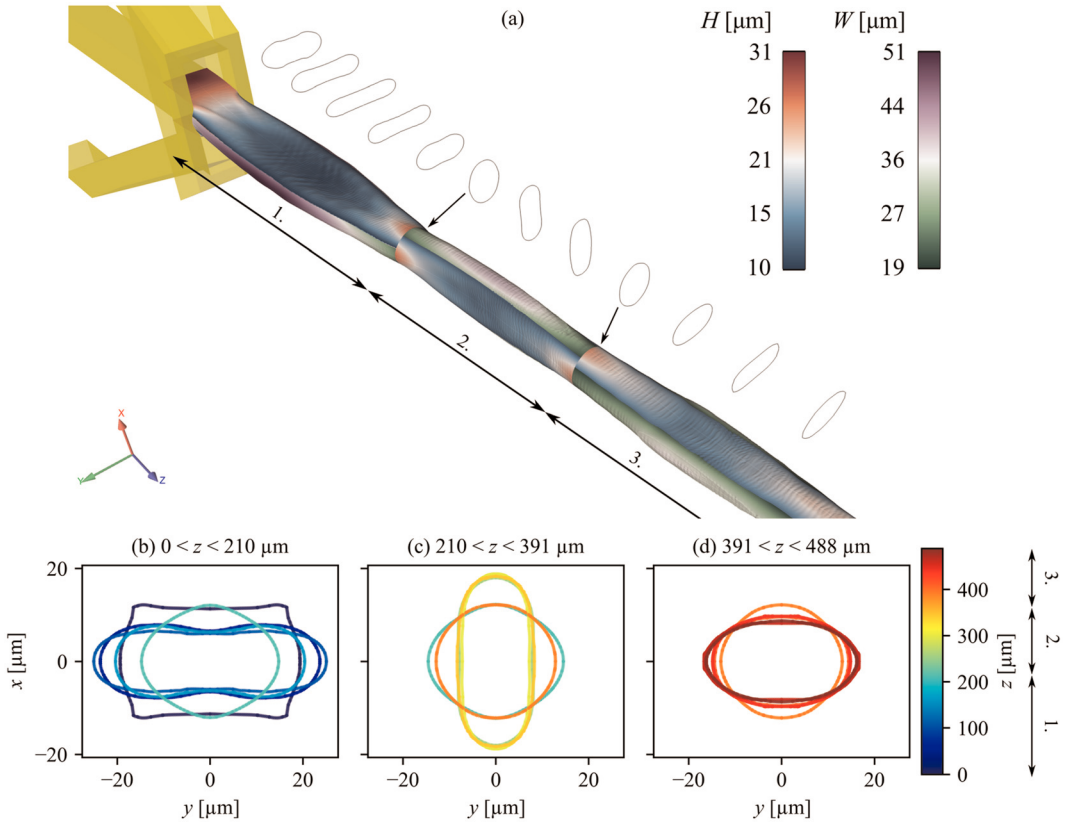

FIG. 9. The width and the thickness of the sheet jet: (a) the thickness and the width with cross-sectional shapes, (b) cross sections of the primary link, (c) cross sections of the secondary link, and (d) cross sections of the tertiary link. Arrows indicate the start of the new links. Numbers 1–3 indicate the orthogonal links of the liquid sheet. Flow rates: helium 12.6 mg min^{-1} and water 600 μl min^{-1}.

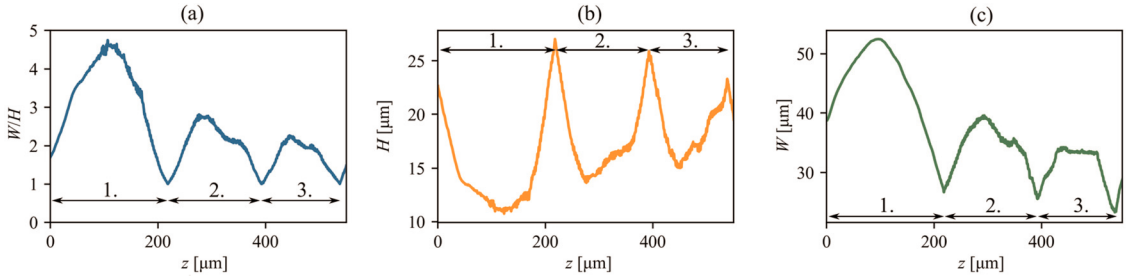

FIG. 10. Aspect ratio, the thickness and the width of the sheet jet along the z axis: (a) aspect ratio thickness/width vs z coordinate, (b) thickness vs z coordinate, and (c) width vs z coordinate. Numbers 1–3 indicate the orthogonal links of the liquid sheet. Flow rates: helium 12.6 mg min^{-1} and water 600 μl min^{-1}.

A. Experimental validation

For quantitative experimental validation, the numerically calculated maximum width and length of the flat sheet jet were compared with experimental measurements. Using the M2 mesh, the maximum width and length are 52.11 and 210.40 μm, respectively. Their experimental uncertainties are of $49.20 \pm 3.29\,\mu$m (width) and $214.60 \pm 14.35\,\mu$m (length). Relative to the experimental values, the numerical width is 6% higher and the length 2% lower. Results with all three meshes, alongside experimental measurements and computational times, are summarized in Table III.

Validation was performed not only locally but also globally, by comparing the entire sheet-jet area obtained from experiments and simulations. Helium–water interfaces were extracted from the respective frames [Fig. 7(c)], and their areas were calculated. Figure 11(a) illustrates the interface extraction, with measurement uncertainty indicated around the experimentally obtained interface. The agreement is excellent: the numerical sheet-jet area (11 371 μm^2) is only 2.8% larger than the experimental area (11 062 μm^2). Furthermore, the intersection between the numerical and experimental areas (10 849 μm^2) covers 98% of the experimental area [Fig. 11(b)], with a nonoverlapping area of 6% (734 μm^2), which falls within the measurement uncertainty.

The 7% uncertainty in the experimental measurement of sheet width and length represents the limits of accuracy of the image processing. The calculated data in the simulations fall within this uncertainty range. Therefore, small quantitative mismatches between the numerical predictions and experimental data do not compromise the validation of overall trends. The agreement is considered robust, as the numerical simulations reproduce the evolution and regime transitions of the primary sheet within the experimental measurement accuracy.

B. Dimensionless numbers

Dimensionless numbers, such as the gas Reynolds number $\mathrm{Re_g} = \dot{m}_g/\mu_g D$, liquid Reynolds number $\mathrm{Re_l} = Q_l\rho_l/\mu_l D$, Weber number $\mathrm{We} = \frac{Q_l\rho_l}{\sigma D^3}$, and capillary number $\mathrm{Ca} = \mathrm{We}/\mathrm{Re_l}$ have been evaluated based on the flow conditions at the end of the gas and liquid capillaries. The material properties used to calculate the dimensionless numbers, such as gasdynamic viscosity μ_g, liquid density ρ_l, liquid dynamic viscosity μ_l, and surface tension σ are provided in Table IV. Characteristic length D is the diameter of the liquid or gas capillary, which equals 30 μm. For the analyzed cases, where helium mass flow $\dot{m}_g$ range $5 - 20$ mg min^{-1} and water volumetric flow Q_l $200 - 600$ μl min^{-1}, the ranges of related dimensionless numbers are provided in Table IV. For a specific case, see Table VI in Appendix B.

C. Physical mechanisms of the regimes

The physical behavior of the sheet formation is investigated to understand why some sheets remain open while the others are closed. In gas-focused and accelerated sheets, the imposed gas flow plays a crucial role in addition to the liquid Weber number, introducing added complexity compared with classical sheet jets formed by impinging liquids.[30] The gas transfers momentum per unit volume $\rho_g v_g$ to the liquid jet, adding a lateral momentum component per unit volume, $\rho_l v_{l,y}$ to the axial liquid momentum per unit volume $\rho_l v_{l,z}$. In the absence of gas focusing, the liquid momentum is purely axial ($v_{l,y} \approx 0$). Gas acceleration, therefore, induces a transverse velocity component $v_{l,y}$, which drives the widening of the sheet into an orthogonal jet. This transverse motion is approximately normal to the rim, so the inertial forces per unit length $\rho_l v_{l,y}^2 R_{rim}$ act in the same normal direction. Opposing this, the restoring action of surface tension σ minimizes the interface area and tends to reestablish a circular jet cross section. Because the sheet's cross section is elongated, the rim curvature is significantly larger than that near the sheet-jet centerline (see Fig. 12), making surface tension particularly effective at the rim. The rim is therefore the region where the balance between inertia $\rho_l v_{l,y}^2 R_{rim}$ and surface tension σ determines whether the sheet remains open or closes. From this balance of forces, the rim Weber number naturally emerges

$$\mathrm{We_{rim}} = \frac{\rho_l v_{l,y,rim}^2 R_{rim}}{\sigma}, \tag{18}$$

TABLE III. Comparison of numerical and experimental results.

	Numerical simulation			
Variable	M1	M2	M3	Experiment
Nr. cells	10 060 641	1 799 578	846 108	
Width (μm)	51.54	52.11	58.00	49.20 ± 3.29
Error/uncertainty (%)	+4.8	+5.9	+17.9	±6.7
Length (μm)	214.67	210.40	198.75	214.60 ± 14.35
Error/uncertainty (%)	−0.03	−2.0	−7.4	±6.7
Computational time (h)	311	110	68	

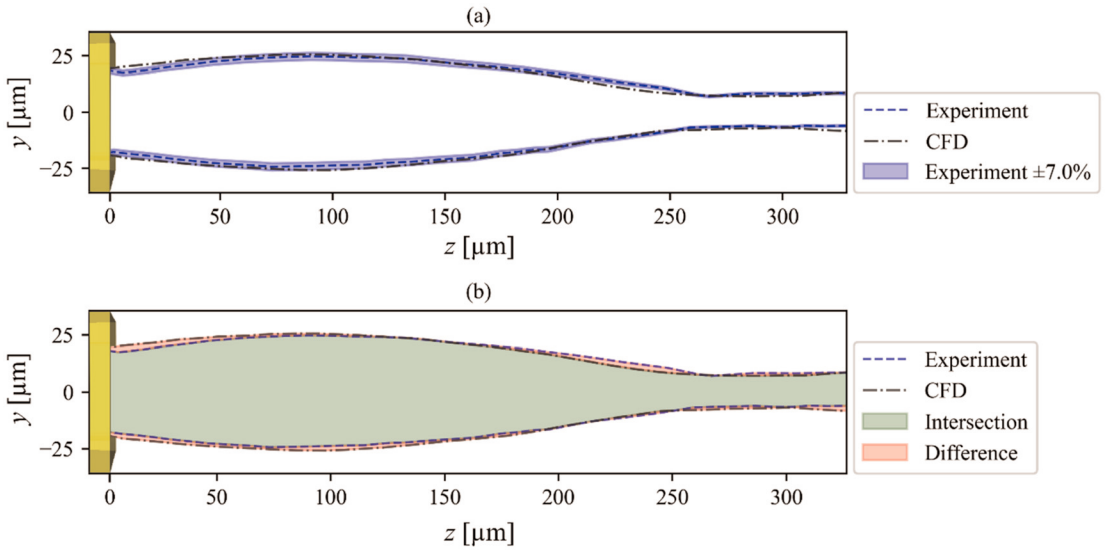

FIG. 11. A comparison of the primary liquid-sheet area from numerical simulation and experimental data: (a) extracted interface of the primary liquid-sheet area from the measurement and from the numerical simulation at the isosurface at a volume fraction 0.5, (b) primary liquid-sheet area comparison between numerical simulation and experimental measurement for helium (12.6 mg min^{-1}) and water (600 μl min^{-1}) flow.

where R_{rim} is the rim radius and $v_{l,y,rim}$ the mean velocity normal to the rim, both obtained by the in-house developed Python algorithm. The main steps of this algorithm are as follows:

(1) **Extraction of the cross sections** at the isosurface $\alpha = 0.5$ in xy plane along the jet axis (z coordinate). Also, the iso-clips $\alpha_l > 0.5$ are extracted with the velocity component values.
(2) **The calculation of the local curvature** κ_i for every point at the interface of the extracted cross section with coordinates (x_i, y_i)

$$\kappa_i = \frac{x_i' y_i'' - y_i' x_i''}{\left(x_i'^2 + y_i'^2\right)^{3/2}}, \tag{19}$$

where x', y', x'', and y'' are the first and second derivatives in x and y directions for i th point along the interface.
(3) **Smoothing the noise of the curvature** κ_i values, which arise from the nonuniform spacing of computational cells due to AMR. The curvature κ_i is smoothed using a discrete convolution over a window of $N = 11$ ($M = 5$) consecutive points. The smoothed curvature $\tilde{\kappa}_i$ is computed as

$$\tilde{\kappa}_i = \sum_{j=-M}^{M} h_j \kappa_{i+j}, \quad N = 2M + 1, \tag{20}$$

where i indexes the point along the interface, j indexes points in the convolution window centered at i, and h_j is the normalized convolution kernel satisfying $\sum_{j=-M}^{M} h_j = 1$.
(4) **Rim region detection**. The rim end is defined as the location at a given cross section, where the smoothed curvature $\tilde{\kappa}_i$ falls below the cross-sectional mean curvature $\tilde{\kappa}_{avg}$. This detection criterion is robust for both characteristic sheet-jet cross-sectional morphologies: peanut-like shape [Fig. 12(a)] and the elliptical shape [Fig. 12(b)].
(5) **Rim radius calculation**. Once the rim region is identified, the rim radius R_{rim} is quantified as $1/\tilde{\kappa}_{avg,rim}$, where $\tilde{\kappa}_{avg,rim}$ denotes the mean smoothed curvature over the rim region.
(6) **Rim velocity calculation.** Inside the rim region, for each computational cell, the velocity in y direction is read. The lateral velocity component $v_{l,y,rim}$ is subsequently averaged within the rim domain (bottom section of the plots in Figs. 12(a) and 12(b), where the $v_{l,y,rim}$ values for each cell inside the rim are shown).
(7) **Local rim Weber number calculation**. With the R_{rim} and $v_{l,y,rim}$ determined, the local rim Weber number $\mathrm{We_{rim}}$ is evaluated along the jet axis by Eq. (18). This is the mean Weber number within the rim for a given cross section.

TABLE IV. Material properties and dimensionless numbers.

μ_g (Pa s)	ρ_l (kg m^{-3})	μ_l (Pa s)	σ(N m^{-1})	$\mathrm{Re_g}$	$\mathrm{Re_l}$	We	Ca
Min. 1.69×10^{-5}	998	1.003×10^{-3}	0.0728	76	91	3.8	0.04
Max. 1.99×10^{-5}				332	336	49	0.15

Figures 13(a)–13(c) show the evolution of sheet width W, thickness H, and $\mathrm{We_{rim}}$ along the sheet for three representative regimes. After leaving the nozzle, the sheet widens and thins, while $v_{l,y,rim}$ increases, raising $\mathrm{We_{rim}}$. As widening continues, the rim curvature increases, strengthening surface tension and reducing $\mathrm{We_{rim}}$.

In the **jet–liquid chain transitional regime** [Fig. 13(a)], surface tension dominates over inertia throughout ($\mathrm{We_{rim}} < 0.1$), preventing full sheet development. As a result, the initial ellipsoidal cross-sectional shape quickly contracts into a cylindrical jet.

In the **liquid chain regime** [Fig. 13(b)], inertia is initially sufficient to form a sheet ($0.1 < \mathrm{We_{rim}} < 1$), but surface tension

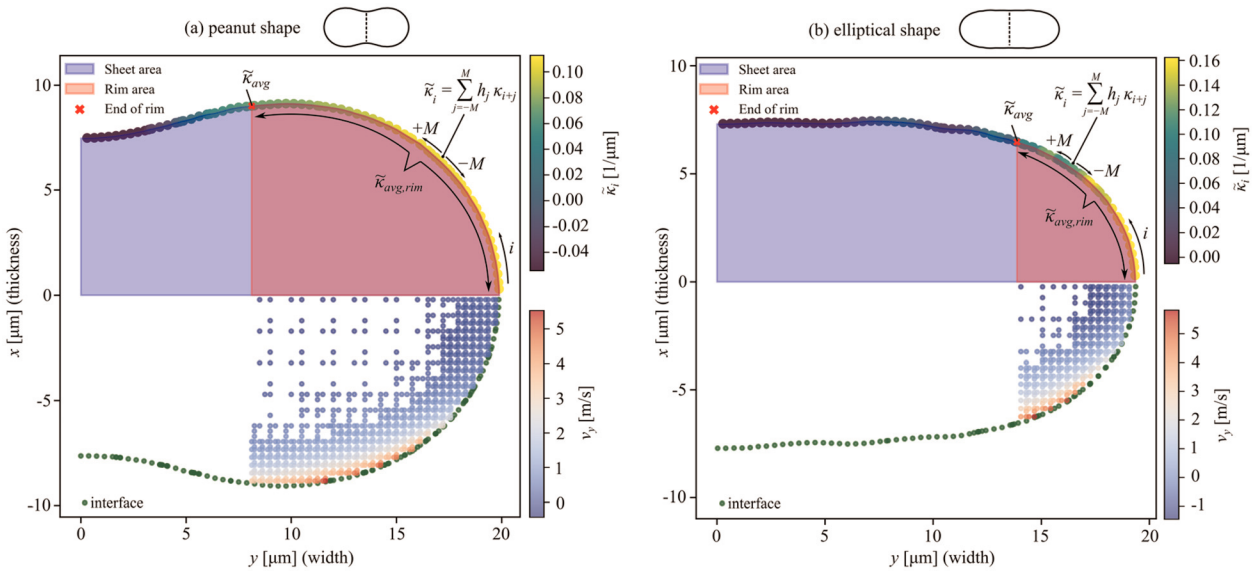

FIG. 12. Visualization of rim detection and determination of rim radius R_{rim} and mean transverse velocity inside the rim $v_{l,y,rim}$ for two characteristic sheet cross-sectional shapes: (a) peanut-like at $z = 14$ μm and (b) elliptical shape at $z = 31$ μm. In each plot, the upper section shows the smoothed curvature $\tilde{\kappa}_i$ along the interface, highlighting the division between the rim and central sheet regions. The lower section presents the transverse velocity $v_{l,y,rim}$ within the rim region.

eventually dominates and causes the rims to bend inward. Since a significant portion of the liquid is transported from the rim into the bulk of the sheet jet, the bulk flow develops a transverse momentum component per unit volume $\rho_l v_{l,x}$, which initiates the formation of the secondary sheet in an orthogonal direction compared to the primary link. At this stage, the sheet thickness begins to increase and eventually becomes comparable to the width, which gets reduced at the same time. At the location where $W/H \approx 1$, the turning point between the primary and secondary links appears, characterized by a nearly circular cross section.

In the **open rim regime** [Fig. 13(c)], rim inertia dominates throughout the sheet evolution, preventing surface tension from redirecting the rim inward. Here, $\mathrm{We_{rim}} > 2$ is consistent with the criterion $\mathrm{We_s} \geq 2$ for absolute instabilities in sheet jets, produced by impinging gas.[49] Under such conditions, the excess inertial forces cause the rim to remain open, ultimately leading to explosive rupture of the sheet. This regime emerges at higher gas flow rates, where liquid inertia within the rim, induced by gas momentum, dominates over the restoring action of surface tension.

The values $\mathrm{We_{rim}} < 0.1$ and $\mathrm{We_{rim}} \geq 2$ represent practical thresholds separating regimes in which rim dynamics are governed by surface tension or inertia, respectively. In all simulated jet–liquid chain transitional cases, $\mathrm{We_{rim}}$ remains below ~0.1 along the entire sheet, indicating that surface tension dominates rim dynamics and prevents sustained lateral sheet growth. Conversely, in all open rim cases, $\mathrm{We_{rim}}$ exceeds 2 at the onset of sheet breakup, reflecting inertia-dominated rim motion that cannot be redirected back by surface tension. These thresholds are therefore not imposed *a priori* but arise consistently from the simulations as markers distinguishing surface tension-controlled transitional regimes from inertia-dominated open rim behavior.

In liquid sheets formed by impinging jets, the liquid viscosity is known to contribute to sheet stabilization.[37] However, in gas-focused liquid sheets, the influence of viscosity on the sheet-jet morphology was previously found to be negligible.[38] This suggests that surface tension and inertia dominate over viscous forces in this configuration. To assess the relative importance of viscosity more rigorously, we evaluated the rim Ohnesorge number, $\mathrm{Oh_{rim}}$, and the rim Capillary number, $\mathrm{Ca_{rim}}$, analogously to the rim Weber number, $\mathrm{We_{rim}}$. The Ohnesorge number quantifies the ratio of viscous forces to the combined effects of inertia and surface tension and is defined here as $\mathrm{Oh_{rim}} = \mu_l/(\rho_l \sigma R_{rim})$. The rim capillary number, $\mathrm{Ca_{rim}} = \mu_l v_{l,y}/\sigma$, expresses the balance between viscous and surface tension forces. The quantities R_{rim} and $v_{l,y}$ are defined in the same manner as for $\mathrm{We_{rim}}$.

Figures 14(a)–14(c) show the evolution of sheet width W, thickness H, $\mathrm{Oh_{rim}}$, and $\mathrm{Ca_{rim}}$ along the sheet for three representative regimes. Both $\mathrm{Oh_{rim}}$ and $\mathrm{Ca_{rim}}$ remain significantly lower than unity across all regimes, confirming that viscosity does not play a dominant role in shaping gas-focused sheet jets. $\mathrm{Oh_{rim}}$ remains nearly constant along the sheet when the rim curvature (and thus R_{rim}) varies only weakly. In open rim regime, however, the rim curvature changes more noticeably, particularly in regions where surface tension is insufficient to turn the rim inward (i.e., where inertia dominates over surface tension $\mathrm{We_{rim}} > 2$). As a result, $\mathrm{Oh_{rim}}$ increases slightly due to higher rim curvature (lower R_{rim}).

The behavior of $\mathrm{Ca_{rim}}$ similarly indicates weak viscous effects. In the transitional jet–liquid chain regime [Fig. 14(a)] and in liquid chain regime [Fig. 14(b)], $\mathrm{Ca_{rim}}$ becomes negative because the transverse velocity $v_{l,y}$ reverses direction. This indicates flow from the rims toward the sheet-jet center. In contrast, $\mathrm{Ca_{rim}} > 0$, in the open rim regime [Fig. 14(c)], is consistent with outward flow within the rims.

With $\mathrm{Oh_{rim}} \ll 1$ and $\mathrm{Ca_{rim}} \ll 1$, we confirm and extend the conclusion of our earlier study[38] that gas-accelerated sheet jets are not sensitive to viscosity changes. Instead, the emergence of distinct liquid-sheet regimes is governed primarily by the balance between inertia and surface tension, captured by $\mathrm{We_{rim}}$.

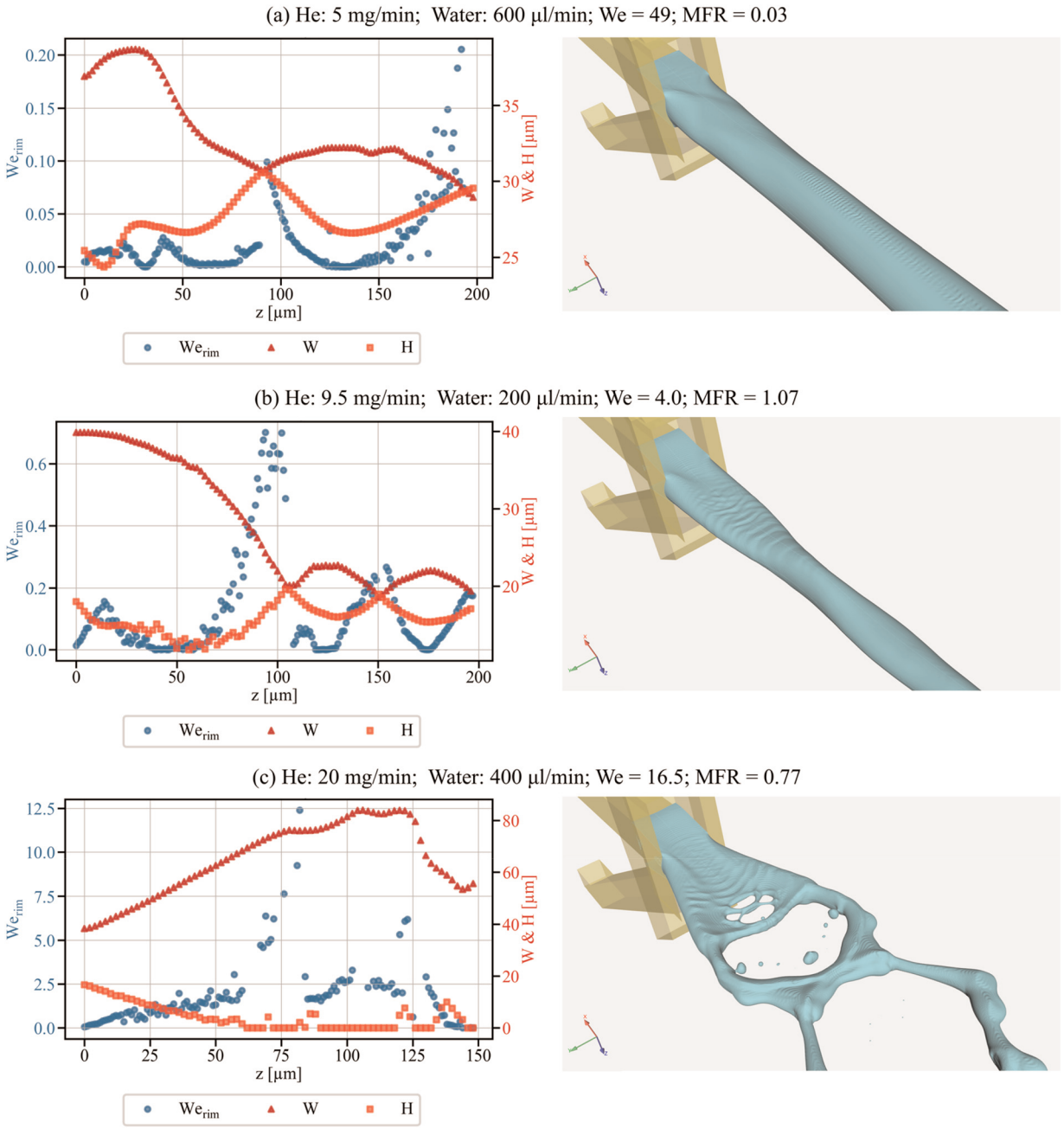

FIG. 13. Evolution of sheet width W, thickness H, and We_{rim} along the sheet for three representative regimes: (a) jet–liquid chain transitional, (b) liquid chain, and (c) open rim. In each subplot, We_{rim} initially rises due to increasing transverse velocity $v_{l,y,rim}$, while subsequent rim curvature growth strengthens surface tension, reducing We_{rim}. For $We_{rim} < 0.1$, a liquid chain does not fully form, whereas $0.1 < We_{rim} < 1$ corresponds to a developed liquid chain. In an open rim regime ($We_{rim} \gg 2$), inertia dominates over surface tension, preventing the rims from bending inward. Each chart is shown together with the corresponding sheet isosurface ($\alpha = 0.5$) to visualize the flow structure.

D. Visualization of liquid chain regime mechanism

The mechanism of liquid chain formation, anticipated by the evolution of We_{rim}, is further clarified through flow visualization. Figure 15(a) shows velocity vectors across sheet-jet cross sections, where the axial velocity $v_{l,z}$ dominates, while the transverse $v_{l,y}$ and vertical $v_{l,x}$ components are smaller but decisive for sheet formation. Their combined action is expressed as the tangential velocity, shown in Fig. 15(b), together with pressure contours and the four characteristic

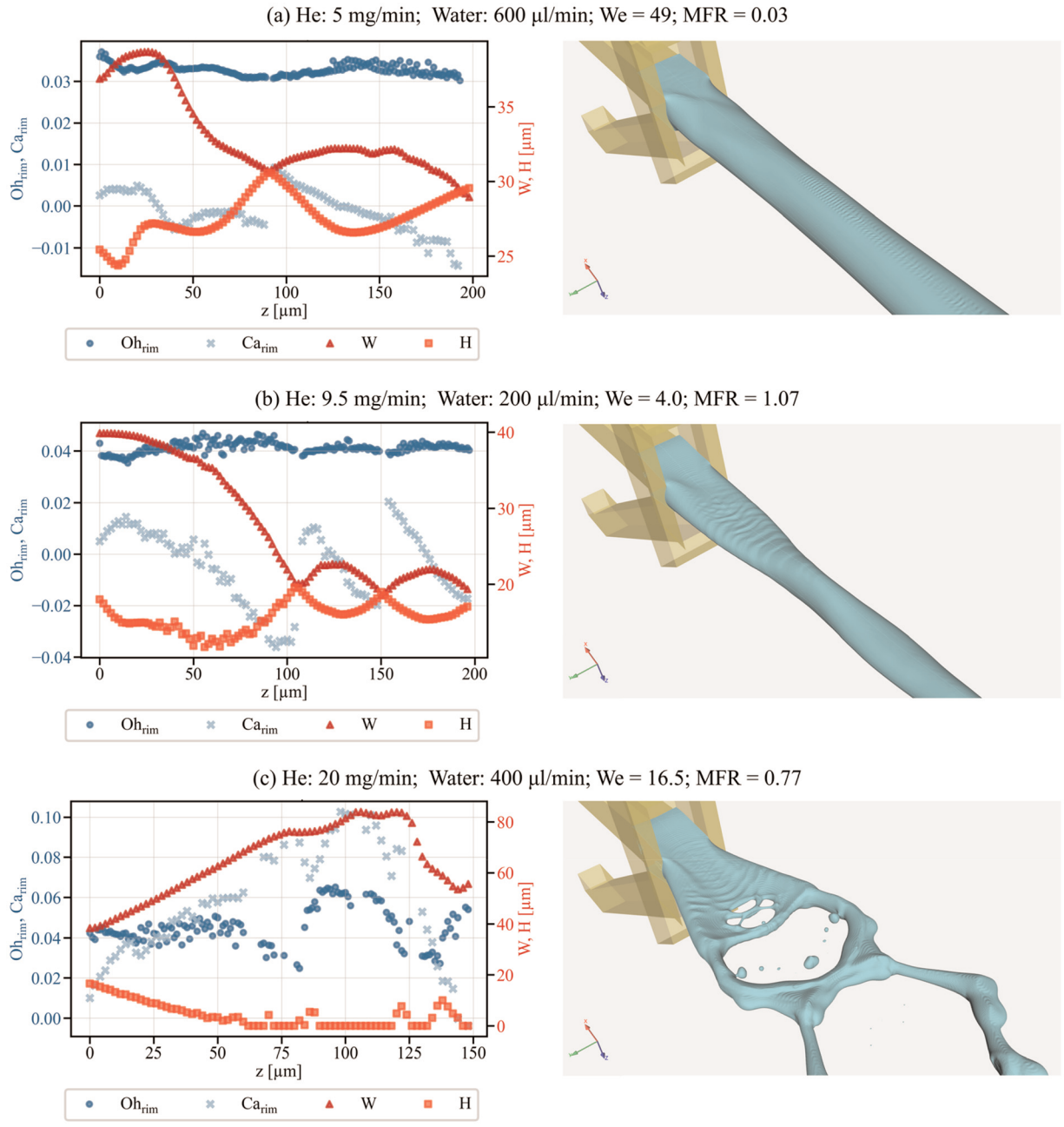

FIG. 14. Evolution of sheet width W, thickness H, rim Ohnesorge number Oh_{rim}, and rim Capillary number Ca_{rim} along the sheet for three representative regimes: (a) jet–liquid chain transitional, (b) liquid chain, and (c) open rim. In all regimes, $Oh_{rim} \ll 1$ and $Ca_{rim} \ll 1$, demonstrating that viscous forces are negligible compared with inertia and surface tension. Regions where the transverse rim velocity becomes negative ($v_{l,y,rim} < 0$) indicate flow directed toward the sheet center and correspond to $Ca_{rim} < 0$. Each plot is shown together with the corresponding sheet isosurface ($\alpha = 0.5$) to illustrate the flow structure.

flow regions. Because the balance of forces evolves gradually, the transitions between regions are not sharply defined, resulting in overlaps, as shown in Fig. 15(b).

The detailed flow dynamic of the liquid chain regime is illustrated in Figs 16–18, where liquid and gas streamlines are shown in each region. Figure 16 shows the locations and orientations of the section views used for the detailed representations in Figs. 17 and 18.

(1) **Region I**: Inside and near the nozzle, the sheath gas transfers momentum flux per unit area $\rho_g v_{g,x}^2$ to the liquid, generating a

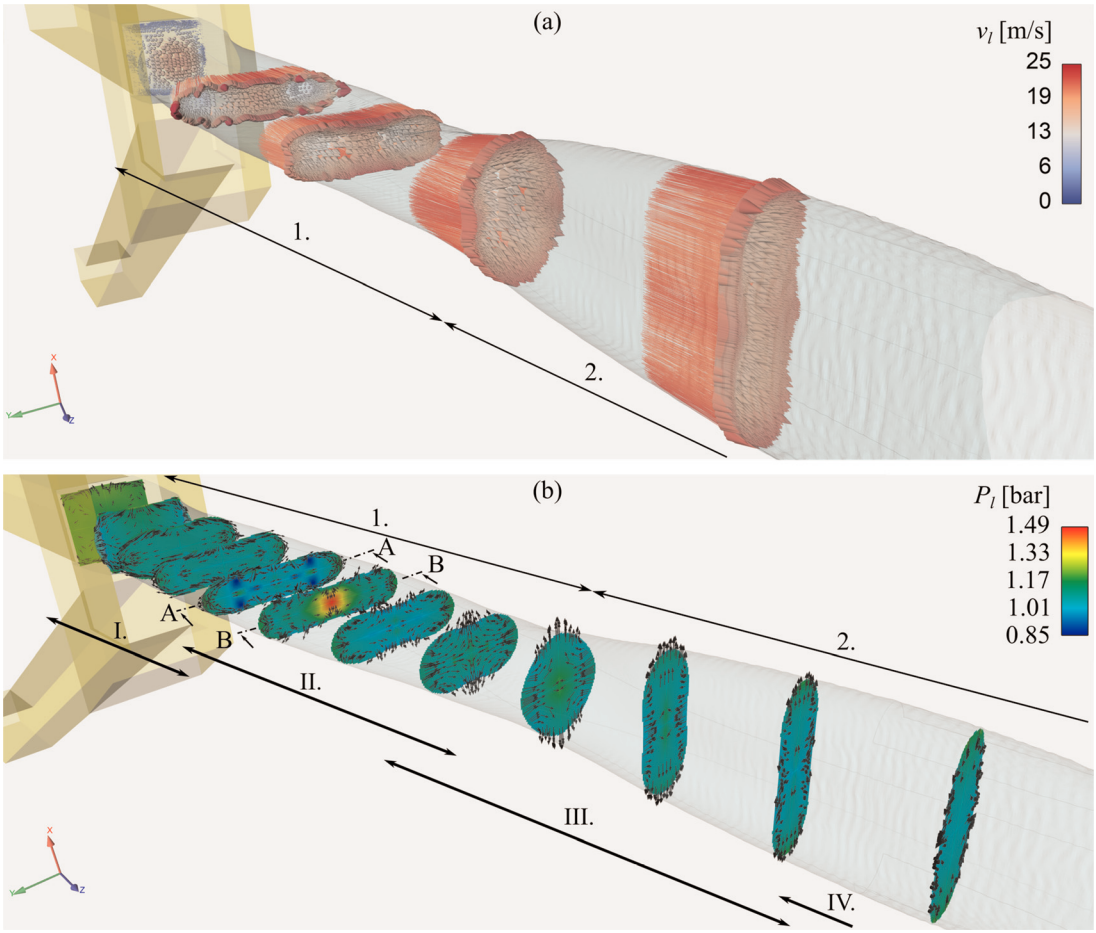

FIG. 15. Velocity vectors: (a) velocity vectors at various cross sections, (b) tangential projection of velocity vectors and pressure contours at various cross sections. Numbers 1–3 indicate the orthogonal links of the liquid sheet. Cross sections A–A and B–B indicate the locations of pressure anomalies, shown in detail in Fig. 19. Roman numerals I–IV mark representative regions illustrating distinct physical flow behaviors. Flow rates: helium 12.6 mg min^{-1} and water 600 μl min^{-1}.

transverse component $\rho_l v_{l,y}^2$. Since $\rho_l v_{l,y}^2 \approx \rho_g v_{g,x}^2$ exceeds the surface tension effect σ/R_{rim} ($\mathrm{We_{rim}} > 0.1$), the sheet expands radially. Figure 17(a) shows liquid and gas streamlines, together with both the conceptual sheath–gas force vectors and the resulting transverse liquid inertia. The radial flow induced by this momentum flux transfer causes the sheet to thin and elongate, while its cross section transforms into an oval shape.

(2) **Region II**: As the jet develops downstream, the sheet cross section becomes increasingly elliptical. This shape change increases the curvature at the wider edges, where the radius of curvature is smaller than at the center. As a result, surface tension grows stronger along the rims and eventually surpasses inertia ($\mathrm{We_{rim}} < 0.1$). The stronger rim surface tension acts to minimize surface area by pulling the rims inward, as illustrated in Fig. 17(b).

(3) **Region III**: When the surface tension bends the rim inward, it pushes liquid streamlines toward the sheet center, where they collide and transfer transverse momentum flux per unit area $\rho_l v_{l,y}^2$ in the vertical direction $\rho_l v_{l,x}^2$.

(4) Figures 18(a) and 18(b) illustrate this process. Figure 18(a) provides a downstream view, while Fig. 18(b) offers an upstream perspective, with the collision point of the streamlines marked as "x." At this stage, transverse momentum flux per unit area $\rho_l v_{l,y}^2$ is progressively reduced while being transferred into vertical momentum flux per unit area $\rho_l v_{l,x}^2$. This momentum flux redistribution is mirrored by the cross-sectional evolution: the elongated oval contracts into a nearly circular shape. At this point, the transverse momentum flux predominantly flows inward while the vertical momentum flux spreads outward, initiating formation of the secondary link. Because $\rho_l v_{l,x}^2$ exceeds σ/R_{rim} ($\mathrm{We_{rim}} > 0.1$), the secondary sheet expands in the vertical direction, orthogonal to the primary link.

(5) **Region IV**: As the secondary sheet continues to expand, differences in curvature of the interface once again lead to unequal surface tension forces. When surface tension overtakes vertical inertia ($\sigma/R_{rim} > \rho_l v_{l,x}^2$, i.e., $\mathrm{We_{rim}} < 0.1$), the rims are pulled

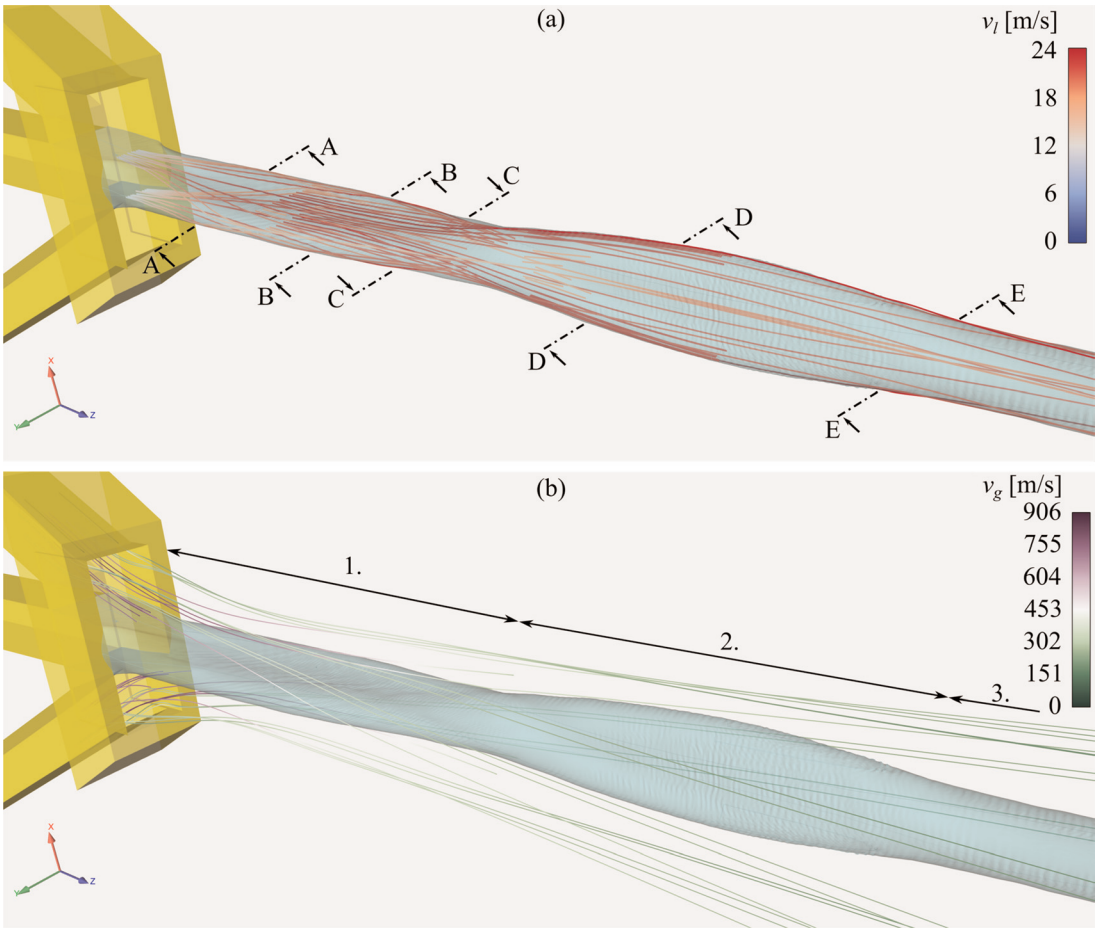

FIG. 16. Liquid (a) and gas (b) streamlines: Cross sections A–E indicate the direction of the view for each of the cross sections, which are shown in detail in Figs. 17 and 18. For clarity, only the most representative streamlines are shown. Numbers 1–3 indicate the orthogonal links of the liquid sheet. Flow rates: helium 12.6 mg min^{-1} and water 600 μl min^{-1}.

inward. This produces a flow pattern analogous to that of Region II but oriented orthogonally, as shown in Fig. 18(c).

Beyond this stage, the sequence of Regions II–IV repeats, giving rise to a tertiary sheet. With each cycle, the sheet alternates between oval and circular cross sections while transverse and vertical momentum components exchange dominance. As the aspect ratio of the cross section progressively decreases, the sheet transitions into a cylindrical jet, which ultimately breaks up through the Rayleigh–Plateau instability. This transformation is accompanied by a gradual redistribution of velocity within the sheet, leading to an increasingly uniform velocity profile downstream [see Fig. 15(a)].

The pressure distribution within the sheet is generally uniform, except at two cross sections where distinct anomalies appear, as seen in Fig. 15(b). Figure 19 highlights these two anomalies and explains their origin.

The first anomaly occurs in Region II, where six localized low-pressure zones appear as streamlines bend inward toward the sheet center [Fig. 19(a)]. This arises because both the rim and the bulk streamlines curve inward toward the jet axis, generating local pressure minima. The resulting inward pull allows the flow to be redirected, as indicated by the arrows in Fig. 19(a). On the inner side of the bend, one such low-pressure zone is circled in Fig. 19(a), marking the location where the streamline changes direction.

The second anomaly appears at the onset of Region III [Fig. 19(b)], where symmetrically converging streamlines meet at the sheet axis. This convergence produces a stagnation-like condition: the inward bulk flow is obstructed, causing a velocity drop and a corresponding pressure rise at the collision point, marked with x. In contrast, the outer edges experience lower pressure, which redirects the bulk flow upward and downward toward the thinner flanks of the sheet. This redistribution of pressure and momentum initiates the vertical expansion of the secondary link.

E. Liquid chain requirements for SFX

In this section, we analyze key requirements for the liquid chain that could be used as a sample delivery system for SFX applications. In

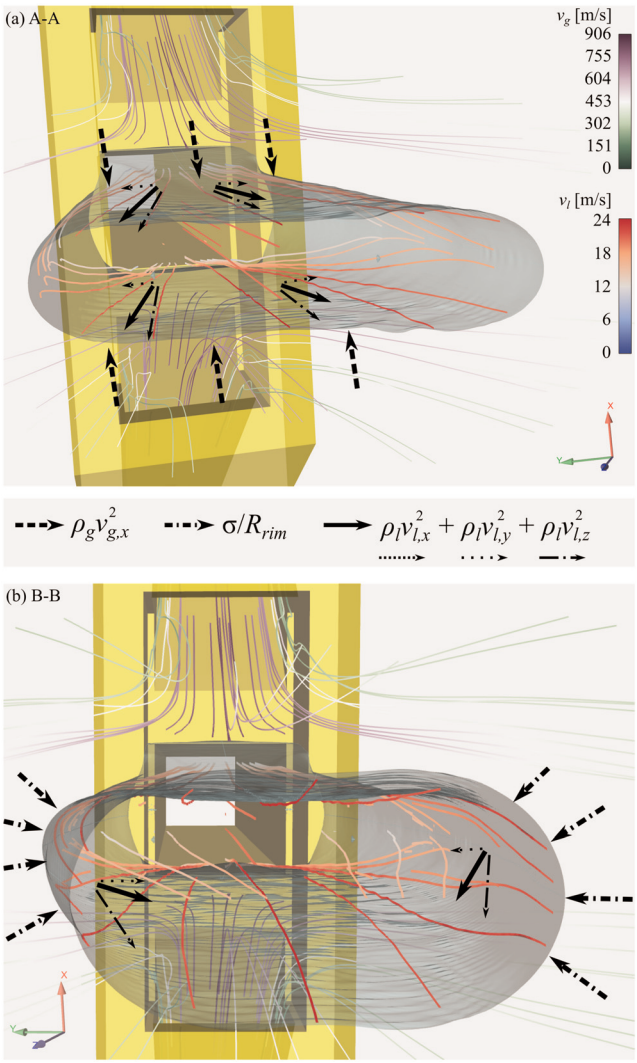

FIG. 17. Gas and liquid streamlines in Regions I and II. (a) Region I, near the nozzle: sheath gas ($\rho_g v_{g,x}^2$) generates transverse liquid inertia ($\rho_l v_{l,y}^2$) exceeding surface tension ($We_{rim} > 0.1$), causing radial expansion and oval cross section. (b) Region II, downstream: increasing oval shape raises curvature at wider edges, making surface tension (σ/R_{rim}) dominant ($We_{rim} < 0.1$) and pulling rims inward, redirecting flow toward the sheet center. Arrows illustrate the different influential forces (see legend). For clarity, only representative streamlines are shown. Flow rates: helium 12.6 mg min^{-1} and water 600 μl min^{-1}.

particular, we are interested in a recirculation-free laminar flow and effective cooling by the expanding sheath gas.

The sheath gas reaches its highest velocity just downstream of the nozzle, where it accelerates and focuses the liquid jet. Figure 20(a) shows the velocity fields of both gas and liquid phases along with line integral convolution (LIC) on the symmetry planes. On the zx plane [Fig. 20(b)], a recirculation zone appears between the liquid and gas streams, indicated by an arrow; such zones are undesirable and can be mitigated by reducing the wall distance between the capillaries. No recirculation is observed on the yz plane [Fig. 20(c)] or within the sheet itself, which should be avoided in liquid-sheet jets for SFX applications. This laminar behavior is further confirmed in Figs. 15(a) and 16–18, where velocity vectors and streamlines show a clear downstream orientation with no visible recirculations or crossing.

In Fig. 21(a), we see the temperature distribution. The sheath gas cools after expanding but this does not lower the temperature of the liquid sheet, ensuring the liquid remains at its original temperature. This is a particularly important effect under vacuum conditions. The compressible nature of the gas flow is highlighted by distribution of Mach numbers in Fig. 21(b). The Mach number is defined as $\mathrm{Ma} = u/c$, where u is the local gas velocity and c is the local speed of sound, calculated for an ideal gas as $c = \sqrt{\gamma RT}$, with γ being the ratio of specific heats, R the specific gas constant and T the local temperature.

F. Liquid chain regime prediction

A local analysis of the flow, which enables the determination of We_{rim} and is achievable only through numerical simulations, helps elucidate the underlying mechanisms governing sheet formation and stability. However, for users aiming to set appropriate flow rates, We_{rim} is not known *a priori*. To address this limitation, we explored how the liquid chain regime can be predicted directly from readily available input parameters, namely, the liquid and gas flow rates and the nozzle geometry.

The liquid chain regime emerges from the crucial balance of inertial, surface tension, and viscous forces. In the present cases, the small capillary numbers Ca (see Table VI in Appendix B) render viscous stresses comparatively weak, so the dominant sheet-driving forces are the inertia of both the gas and liquid, together with surface tension. These effects can be quantified via the momentum flux ratio MFR and the Weber number We

$$\mathrm{MFR} = \frac{\rho_g v_{g,x}^2}{\rho_l v_{l,z}^2}, \tag{21}$$

$$\mathrm{We} = \frac{\rho_l v_{l,z}^2 D_l}{\sigma}, \tag{22}$$

where ρ_g and ρ_l are gas and liquid densities, $v_{g,x}$ is the gas velocity component normal to the jet, $v_{l,z}$ is the axial liquid velocity, $v_{l,y}$ is the induced transverse liquid velocity, and D_l is the diameter of the liquid capillary. The relevant material properties and flow characteristics are extracted from simulations and averaged on an XY plane located at the exit ($Z = -40\,\mu$m) of the gas and liquid capillaries before the mixing zone inside the nozzle. However, they can also be calculated from the flow rates and nozzle geometry.

By fitting the numerical simulation data with a power-law combination of MFR and We, we identify the range corresponding to the liquid chain regime as

$$1.5 \lesssim \mathrm{MFR}\,\mathrm{We}^{0.84} \lesssim 4. \tag{23}$$

For values above this range, the open rim regime develops, while for values below it, the jet does not fully transform into a liquid chain. The limiting values in Eq. (23) were interpolated from simulation data at the boundaries between flow regimes and may vary slightly depending on the dataset. A more precise determination would require additional simulations in the transitional regions. The boundaries of all regimes are shown in Fig. 22.

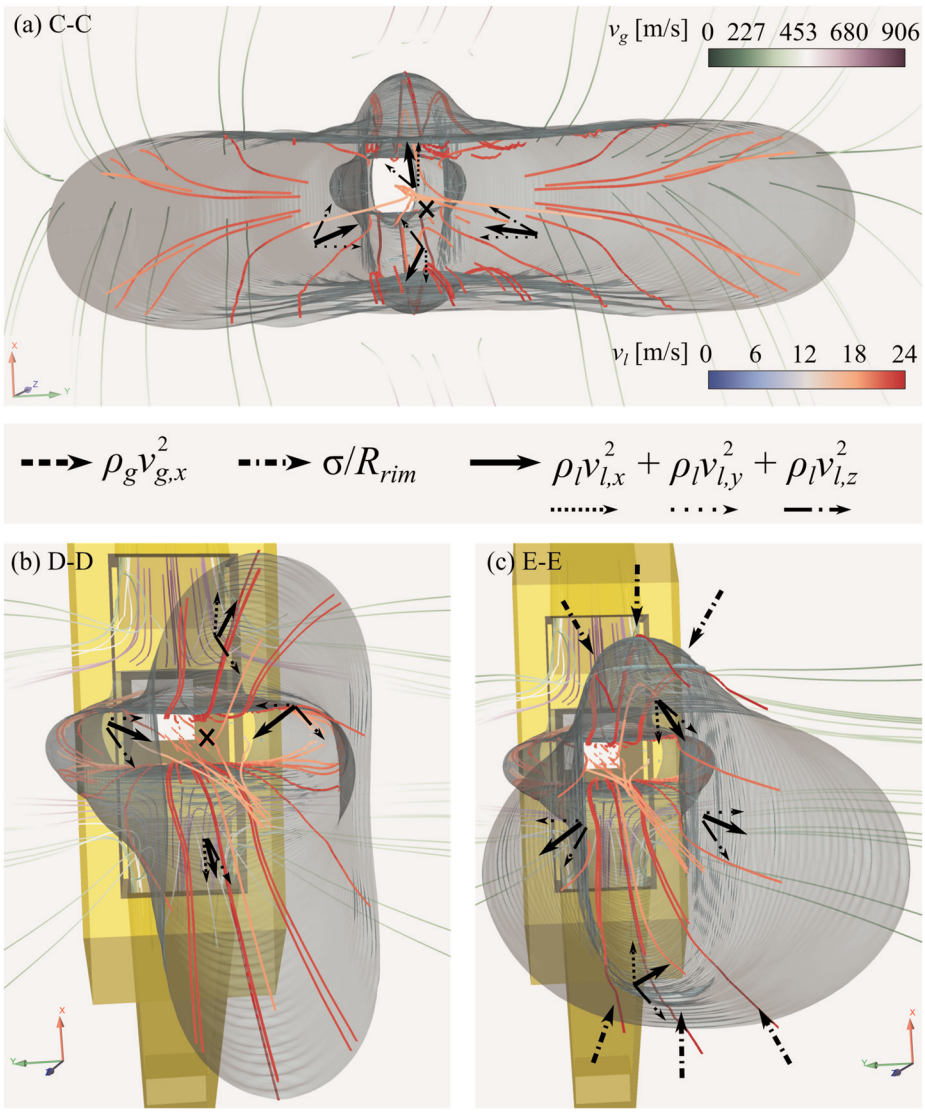

FIG. 18. Gas and liquid streamlines in Regions II–IV. (a) Region III, downstream view: inward-moving rims collide at the center, transferring transverse ($\rho_l v_{l,y}^2$) to vertical ($\rho_l v_{l,x}^2$) momentum flux per unit area forming the secondary link. Collision point marked x. (b) Region III, upstream view: same process as (a), showing radial redirection. (c) Region IV: curvature differences along the secondary sheet rims cause surface tension (σ/R_{rim}) to dominate ($We_{rim} < 0.1$) pulling rims inward and generating a flow pattern orthogonal to Region II. Arrows illustrate the different influential forces (see legend). For clarity, only representative streamlines are shown. Flow rates: helium 12.6 mg min^{-1} and water 600 μl min^{-1}.

The condition in Eq. (23) has a practical significance, as both the MFR and We can be expressed solely in terms of process parameters. The transverse gas velocity component can be calculated as $v_{g,x} = \dot{m}_g \sin\theta \rho_g^{-1} D_g^{-2}$ and the axial liquid velocity as $v_{l,z} = Q_l D_l^{-2}$, where θ s the angle between the gas and liquid capillaries, and D_g and D_l are their respective diameters. Consequently, the MFR and We can be directly estimated from the gas and liquid flow rates, material properties, and nozzle geometry

$$\mathrm{MFR} = \frac{\dot{m}_g^2 \sin^2\theta}{\rho_g \rho_l Q_l^2}, \tag{24}$$

$$\mathrm{We} = \frac{\rho_l Q_l^2}{\sigma D^3}. \tag{25}$$

G. Sheet thickness, width, and length

For all simulated cases, the primary sheet thickness, width, and length were extracted as explained in Fig. 10. The results are shown in Fig. 23. The sheet thickness is defined as the minimum local thickness, the width as the maximum span, and the length as the distance from the nozzle outlet to the end of the primary link—or, in the case of the open rim regime, to the end of the sheet jet.

The sheet length increases approximately linearly with the liquid flow rate across all regimes [Fig. 23(a)]. In the open rim regime, this growth is steeper than in the liquid chain regime. Moreover, the length exhibits pronounced oscillations due to the chaotic nature of breakup, whereas in the liquid chain regime, the length remains stable. As a

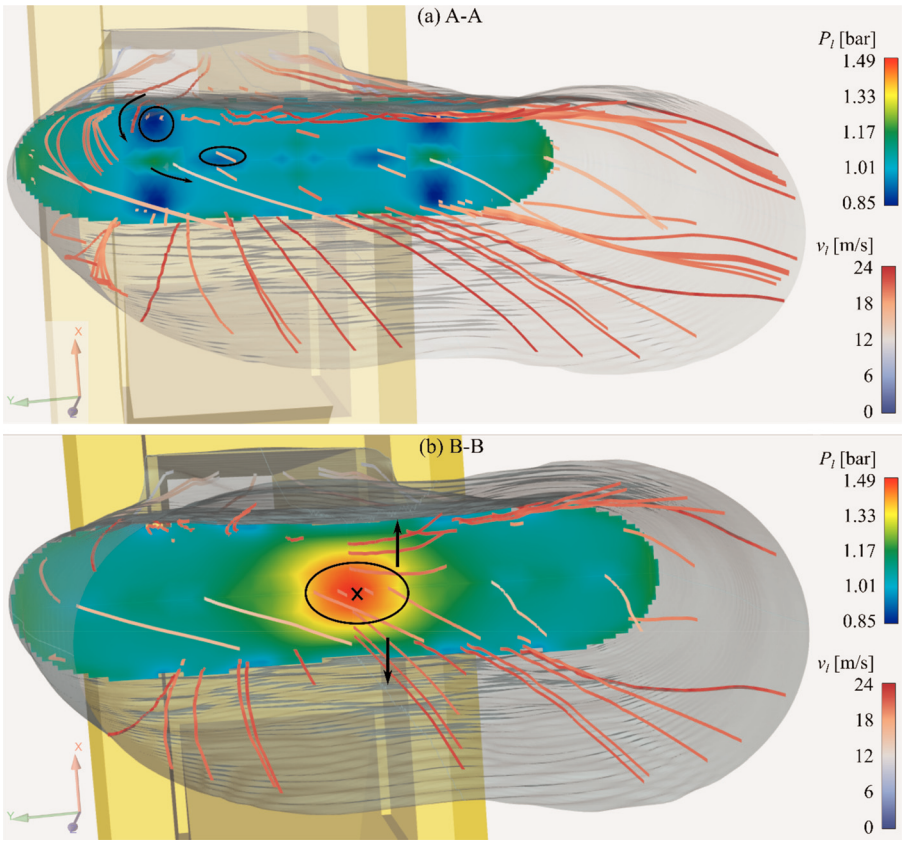

FIG. 19. Pressure contours of the liquid chain and streamlines (a) pressure contours and liquid streamlines at A-A section and (b) pressure contours and liquid streamlines at B-B section. The location of the cross sections A-A and B-B is marked in Fig. 15(b). Flow rates: helium 12.6 mg min^{-1} and water 600 μl min^{-1}.

result, error bars (standard deviation) in Fig. 23(a) are negligible for the liquid chain but significant for the open rim.

In contrast, the sheet width W only weakly depends on the liquid flow rate and remains nearly constant, except at the lowest liquid flow rates [Fig. 23(b)]. The gas flow rate exerts a much stronger influence on the sheet width, as it transfers transverse momentum flux per unit area of order $\rho_g v_{g,x}^2$ to the liquid jet. For a fixed gas flow rate, this contribution remains nearly constant. The total liquid momentum flux per unit area can be expressed as $\rho_l v_{l,x}^2 + \rho_l v_{l,y}^2 + \rho_l v_{l,z}^2$, where the streamwise component $\rho_l v_{l,z}^2$ dominates, the transverse component satisfies $\rho_l v_{l,y}^2 \approx \rho_g v_{g,x}^2$, and the vertical (in the direction of sheet thickness) component $\rho_l v_{l,x}^2 \ll \rho_l v_{l,y}^2 \ll \rho_l v_{l,z}^2$. Increasing the liquid flow rate Q_l therefore primarily increases $\rho_l v_{l,z}^2$, while $\rho_l v_{l,y}^2$ remains nearly unchanged for a fixed gas flow rate. Consequently, the ratio $\rho_l v_{l,y}^2 / \rho_l v_{l,z}^2$ decreases with increasing Q_l, and the sheet can no longer be widened significantly. A similar trend is observed in the open rim regime, where the width fluctuates chaotically, but the mean value remains approximately constant.

The sheet thickness H exhibits distinct behavior across regimes [Fig. 23(c)]. In the liquid chain regime, the thickness increases with increasing Q_l. In contrast, in both the transitional regime between jet and liquid chain and in the open rim regime, the thickness remains nearly constant with increasing Q_l, as a limiting value is reached. In the first case, this minimum thickness is governed by surface tension forces, which dominate over inertia ($\mathrm{We_{rim}} < 0.1$) and suppress further stretching, resulting in a relatively thick cross section. In the second, the minimum thickness is instead dictated by inertial forces that drive sheet breakup ($\mathrm{We_{rim}} > 2$). Overall, increasing the gas flow rate $\dot{m}_g$ yields thinner sheets, since the imparted transverse momentum $\rho_l v_{l,y}^2$ widens the sheet and thereby reduces its thickness.

Since the sheet thickness in the open rim regime approaches the mesh size, it is important to emphasize that numerical resolution limitations do not cause the observed breakup. For the baseline mesh M2 (min. cell size 375 nm), the minimum sheet thickness of ~1.2–1.7 μm is resolved by 4–6 cells, exceeding the commonly accepted requirement to avoid artificial breakup of thin liquid films. The case with the thinnest thickness ($\dot{m}_g = 20$ mg/min, $Q_l = 200$ μl/min) was additionally simulated using a finer mesh M1 (minimum cell size 188 nm) to verify grid convergence, and the open rim regime persisted without qualitative changes. Due to the high computational cost, mesh M1 was applied only to this case. Furthermore, the breakup morphology observed in the simulations matches experimental observations, and the physical nature of the breakup is supported by rim Weber numbers exceeding 2, indicating inertia-dominated behavior.

V. CONCLUSION

This study presents an experimentally validated numerical analysis of gas-accelerated flat sheet jets across multiple regimes, including transitional jet-liquid chain, liquid chain, and open rim. The simulations show high fidelity in predicting jet characteristics. For mesh M2 (min. cell size 375 nm, 1.8×10^6 cells), the primary link area and maximum width are overestimated by 6%, while jet length is

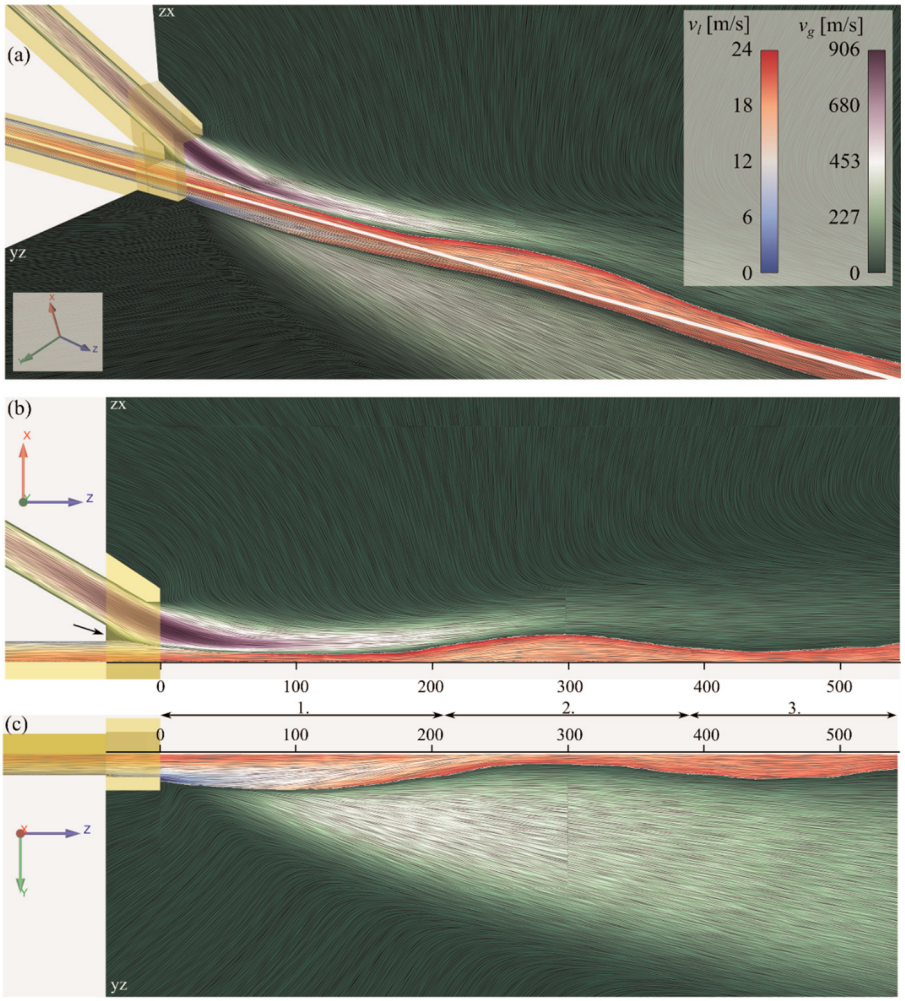

FIG. 20. Helium v_g and water velocity v_l. (a) Velocity contours and LIC at zx and yz symmetry planes, (b) velocity contours and LIC at zx plane, and (c) velocity contours and LIC at yz plane. Numbers 1–3 indicate the orthogonal links of the liquid sheet. Flow rates: helium 12.6 mg min^{-1} and water 600 μl min^{-1}.

underestimated by 2%, all within the 7% experimental measurement uncertainty. Finer mesh M1 (min. cell size 188 nm, 10×10^6 cells) improves accuracy but more than doubles computational cost. A grid convergence study confirms that mesh M2, with two adaptive refinement levels, provides sufficient resolution, with at least three nonadaptive cells required across the thinnest section.

Analysis of the sheet jet reveals four distinct flow regions, governed by the interplay of sheath gas momentum, liquid inertia, and surface tension. The rim dynamics, particularly rim curvature and the transverse velocity induced by the gas, control the sheet's expansion and closure. Introducing the local rim Weber number We_{rim} provides a quantitative criterion for regime identification: $We_{rim} < 0.1$ corresponds to the jet–liquid chain transitional regime, $0.1 < We_{rim} < 1$ defines the liquid chain regime, and $We_{rim} > 2$ marks the open rim regime. Furthermore, the liquid chain regime can be predicted directly from nozzle geometry and flow rates through a relation $1.5 \lesssim \mathrm{MFR}\, We^{0.84} \lesssim 4$, offering a practical tool for experimental design.

Both liquid and gas flow rates govern the primary sheet characteristics. Sheet length increases roughly linearly with liquid flow rate across all regimes, with steeper growth and greater fluctuations in the open rim regime due to chaotic breakup. In contrast, the liquid chain maintains a stable length. The sheet width is less sensitive to liquid flow rate but is strongly controlled by the gas flow rate. Sheet thickness shows distinct regime-dependent behavior: in the liquid chain, it increases with liquid flow, whereas in both the transitional regime between jet and liquid chain and in the open rim regime, thickness remains nearly constant, determined either by surface tension ($We_{rim} < 0.1$) or by inertial breakup ($We_{rim} > 2$). Higher gas flow rates generally reduce thickness, as the additional transverse momentum widens the sheet.

The flow within the liquid chain exhibits clear laminar characteristics, a crucial requirement for SFX applications, ensuring stable and uniform sample delivery. A small recirculation zone is observed in the gas flow near the liquid–gas capillary interface inside the nozzle, which could disrupt laminar conditions. To mitigate this effect, reducing the wall distance between the liquid and gas capillaries can be useful.

Taken together, these results advance the understanding of gas-accelerated sheet-jet dynamics, providing critical guidance for nozzle optimization in applications ranging from SFX to spectroscopy. They

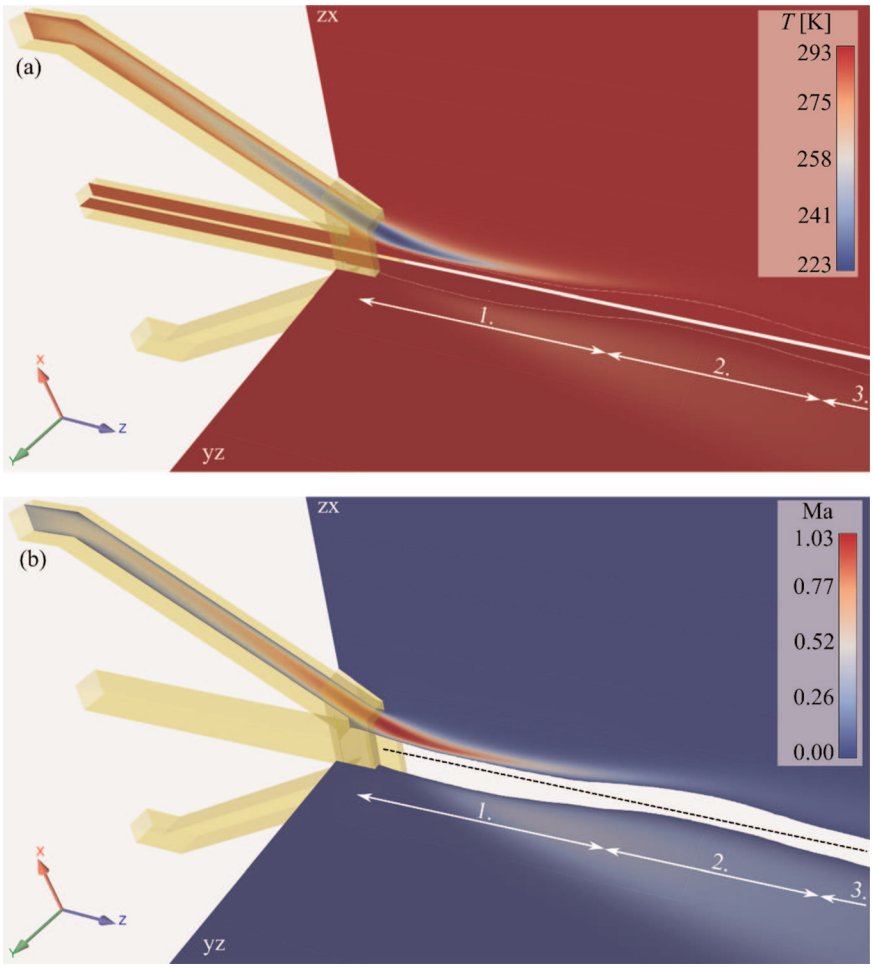

FIG. 21. Temperature and Mach number (a) temperature contours on zx and yz plane for both phases, (b) Mach number contours on zx and yz plane. Numbers 1–3 indicate the orthogonal links of the liquid sheet. Flow rates: helium 12.6 mg min^{-1} and water 600 μl min^{-1}.

also lay the foundation for future studies under vacuum conditions, where the sheet thickness is expected to be significantly smaller.

ACKNOWLEDGMENTS

Funding for this research was provided by the Centre for Free-Electron Laser Science (CFEL) under the project: Innovative Methods for Imaging with the use of X-ray Free-Electron Laser (XFEL) and Synchrotron Sources: Simulation of Gas-focused Micro-jets; and the Slovenian Grant and Innovation Agency (ARIS) within core funding P2-0162, Project No. J2-4477, and the Young Researcher Program. This work was also partly funded by the Cluster of Excellence "CUI: Advanced Imaging of Matter" of the Deutsche Forschungsgemeinschaft (DFG): EXC 2056, Project ID: 390715994.

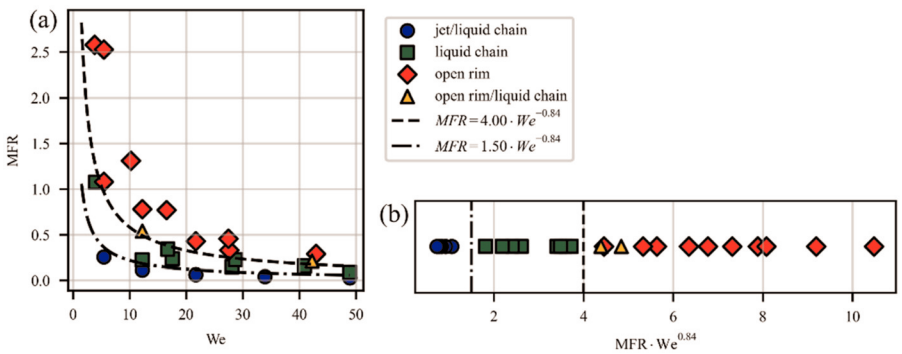

FIG. 22. Flow regimes of gas-accelerated liquid sheets in nondimensional form. (a) Flow regimes in the MFR–We plane, with fitted boundaries separating the jet–liquid chain transitional, liquid chain, and open rim regimes. (b) The same data plotted against the combined scaling law MFR We$^{0.84}$, highlighting the range 1.5 $\lesssim$ MFR We$^{0.84}$ $\lesssim$ 4 corresponding to the liquid chain regime.

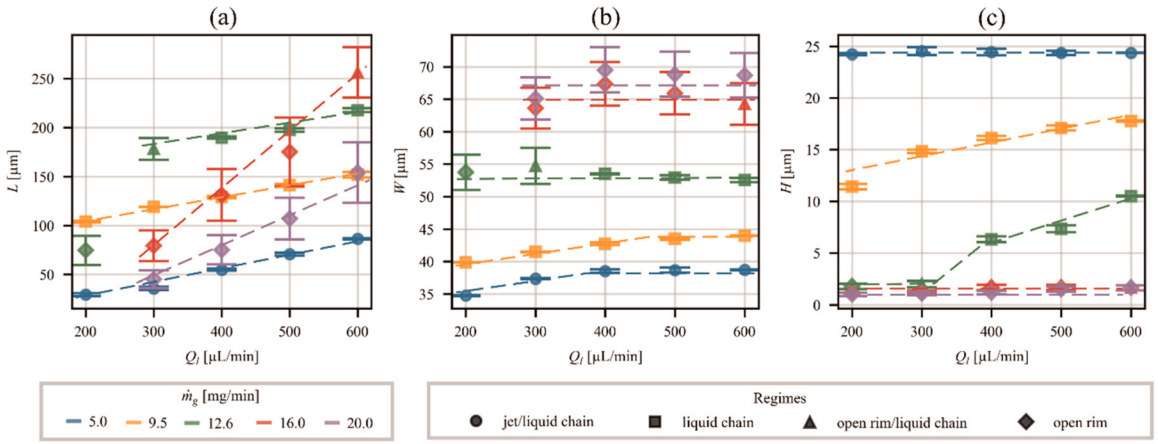

FIG. 23. Dimensions of primary sheet across all simulated cases: (a) length L, (b) width W, and (c) thickness H. All quantities are plotted against the liquid flow rate Q_l for different gas flow rates $\dot{m}_g$. Distinct markers denote different flow regimes, and error bars represent the standard deviation of the dimension averaged over the fully developed sheet.

The authors would like to thank Henry N. Chapman from DESY (Hamburg, Germany), a member of the Helmholtz Association HGF, for the opportunity to perform validation experiments at CFEL (Hamburg, Germany).

AUTHOR DECLARATIONS

Conflict of Interest

The authors have no conflicts to disclose.

Author Contributions

Krištof Kovačič: Conceptualization (equal); Data curation (lead); Formal analysis (lead); Investigation (lead); Methodology (lead); Software (lead); Validation (equal); Visualization (lead); Writing – original draft (lead); Writing – review & editing (equal). **Rizwan Zahoor:** Conceptualization (supporting); Formal analysis (equal); Investigation (equal); Methodology (equal); Visualization (equal); Writing – original draft (supporting); Writing – review & editing (equal). **Jernej Kušar:** Conceptualization (supporting); Data curation (supporting); Software (supporting); Validation (lead). **Sasa Bajt:** Conceptualization (equal); Formal analysis (equal); Funding acquisition (equal); Investigation (supporting); Methodology (supporting); Project administration (equal); Resources (equal); Supervision (supporting); Writing – review & editing (equal). **Bozidar Sarler:** Conceptualization (equal); Formal analysis (equal); Funding acquisition (equal); Investigation (equal); Methodology (equal); Project administration (equal); Resources (equal); Supervision (lead); Writing – review & editing (lead).

DATA AVAILABILITY

The data that support the findings of this study are available from the corresponding author upon reasonable request.

APPENDIX A: MEASUREMENT UNCERTAINTY

The standard uncertainty of the liquid-sheet length is determined with the following equation, which is derived from Eq. (1) after partial derivation:

$$u(L) = \sqrt{C^2 u^2(L_{px}) + L_{px}^2 u^2(C)}, \tag{A1}$$

where $u(L_{px})$ and $u(C)$ are uncertainties of the liquid sheet's length measured in the image and the calibration constant, respectively. They are defined with the following equations:

$$u(L_{px}) = \sqrt{u_{reproj}^2(L_{px}) + u_{bin}^2(L_{px}) + u_{res}^2(L_{px}) + u_A^2(L_{px})}, \tag{A2}$$

TABLE V. Expanded, standard uncertainty, and uncertainties of its sources.

u_{bin} (px)	u_{res}(px)	$u(L_{ref})$(μm)	$u_A(P_{ref})$(px)	$u(P_{ref})$ (px)	$u(C)$(μm px^{-1})
2.31	0.29	0.12	7.19	7.56	0.0066
L (μm)	$u_A(L)$ (px)	$u(L_{px})$ (px)	$u(L)$ (μm)	$U(L)$ (μm)	$U_r(L)$ (%)
214.60	12.90	13.11	7.17	14.35	6.69
W (μm)	$u_A(W)$ (px)	$u(W_{px})$ (px)	$u(W)$ (μm)	$U(L)$ (μm)	$U_r(W)$ (%)
49.20	1.89	3.00	1.64	3.29	6.68

TABLE VI. Dimensionless numbers for analyzed cases.

$\dot{m}_g$ (mg min^{-1})	Q_l (μl min^{-1})	MFR	We	$\mathrm{Re_l}$	$\mathrm{Re_g}$	Ca
5.00	200	0.26	5.4	109	76	0.05
5.00	300	0.11	12	163	76	0.07
5.00	400	0.06	22	218	76	0.10
5.00	500	0.04	34	272	76	0.12
5.00	600	0.03	49	326	76	0.15
9.50	200	1.07	4.0	93	145	0.04
9.50	300	0.22	12	163	145	0.07
9.50	400	0.24	18	195	145	0.09
9.50	500	0.15	28	247	145	0.11
9.50	600	0.08	49	326	145	0.15
12.6	200	1.08	5.4	108	195	0.05
12.6	300	0.54	12	163	196	0.06
12.6	400	0.34	17	191	195	0.09
12.6	500	0.22	29	250	195	0.12
12.6	600	0.16	41	299	195	0.14
16.0	200	2.58	3.8	91	254	0.04
16.0	300	0.78	12	163	254	0.07
16.0	400	0.43	22	217	251	0.10
16.0	500	0.33	28	245	251	0.11
16.0	600	0.21	42	303	251	0.14
20.0	200	2.53	5.5	109	311	0.05
20.0	300	1.31	10	149	322	0.07
20.0	400	0.77	17	190	319	0.09
20.0	500	0.46	28	245	318	0.11
20.0	600	0.29	43	305	317	0.14

$$u(C) = \sqrt{\left(\frac{1}{P_{ref}}\right)^2 u^2(L_{ref}) + \left(-\frac{L_{ref}}{P_{ref}^2}\right)^2 u^2(P_{ref})}. \quad \text{(A3)}$$

Since the liquid sheet is located in the center of the image, we neglected the reprojection error due to the camera distortion, meaning u_{reproj} equals zero. Uncertainties due to binarization u_{bin} and camera resolution u_{res} are type B uncertainties of the rectangular probability distribution. We estimate that the binarization error is within two pixels per boundary, and the error due to camera resolution is within one pixel. Since we measured the distance manually, we repeated these measurements 20 times. Therefore, there is also an uncertainty of type A $u_A(L_{px})$, which is a standard deviation of the collected measurements. The uncertainty of calibration constant further depends on the following uncertainties of reference object measurements in image $u(P_{ref})$ and its known distance $u(L_{ref})$. They are defined as

$$u(P_{ref}) = \sqrt{u_{reproj}^2(P_{ref}) + u_{bin}^2(P_{ref}) + u_{res}^2(P_{ref}) + u_A^2(P_{ref})}, \quad \text{(A4)}$$

$$u(L_{ref}) = u_B(L_{ref}), \quad \text{(A5)}$$

where $u(P_{ref})$ is analogically calculated as $u(L_{px})$ and $u(L_{ref})$ is equal to the uncertainty due to the printer resolution (200 nm) of type B $u_B(L_{ref})$. Table V illustrates the uncertainties associated with each source type.

TABLE VII. Quantities to evaluate dimensionless numbers.

$\dot{m}_g$ (mg min^{-1})	Q_l (μl min^{-1})	$v_{l,z}$ (m s^{-1})	$v_{g,x}$ (m s^{-1})	$v_{g,mag}$ (m s^{-1})	ρ_g (kg m^{-3})	μ_g (kg m^{-1} s^{-1})
5.00	200	3.6	136	272	0.181	1.95×10^{-5}
5.00	300	5.5	136	271	0.181	1.95×10^{-5}
5.00	400	7.3	135	270	0.181	1.95×10^{-5}
5.00	500	9.1	135	270	0.182	1.95×10^{-5}
5.00	600	10.9	135	270	0.182	1.95×10^{-5}
9.50	200	3.1	210	442	0.202	1.87×10^{-5}
9.50	300	5.5	220	442	0.198	1.88×10^{-5}
9.50	400	6.5	222	442	0.204	1.86×10^{-5}
9.50	500	8.3	220	442	0.204	1.86×10^{-5}
9.50	600	10.9	220	442	0.205	1.87×10^{-5}
12.6	200	3.6	256	535	0.218	1.82×10^{-5}
12.6	300	5.5	256	535	0.220	1.81×10^{-5}
12.6	400	6.4	256	535	0.218	1.82×10^{-5}
12.6	500	8.4	256	535	0.218	1.82×10^{-5}
12.6	600	10.0	261	535	0.225	1.82×10^{-5}
16.0	200	3.0	317	624	0.237	1.75×10^{-5}
16.0	300	5.5	309	612	0.242	1.75×10^{-5}
16.0	400	7.3	303	602	0.245	1.76×10^{-5}
16.0	500	8.2	299	596	0.248	1.77×10^{-5}
16.0	600	10.1	297	593	0.249	1.77×10^{-5}
20.0	200	3.6	358	670	0.262	1.69×10^{-5}
20.0	300	5.0	348	685	0.267	1.70×10^{-5}
20.0	400	6.3	335	663	0.276	1.72×10^{-5}
20.0	500	8.2	330	655	0.279	1.73×10^{-5}
20.0	600	10.2	328	652	0.280	1.73×10^{-5}

APPENDIX B: DIMENSIONLESS NUMBERS

The dimensionless numbers in Table VI are calculated from the extracted averaged quantities, listed in Table VII, which are obtained at the end of the gas or liquid capillary inside the nozzle, immediately before the mixing section of the nozzle. The material properties of the liquid are constant, density $\rho_l = 998\,\mathrm{kg\,m^{-3}}$, viscosity $\mu_l = 1.003 \times 10^{-3}\,\mathrm{kg\,m^{-1}s^{-1}}$, and surface tension $\sigma = 0.0728\,\mathrm{N\,m^{-1}}$.

REFERENCES

[1] H. N. Chapman, P. Fromme, A. Barty, T. A. White, R. A. Kirian, A. Aquila, M. S. Hunter, J. Schulz, D. P. DePonte, and U. Weierstall, "Femtosecond X-ray protein nanocrystallography," Nature **470**, 73–77 (2011).

[2] J. Knurr, P. Hemberger, P. Ascher, S. Augustin, D. J. Hoffman, G. Knopp, S. Menzi, Z. Sun, S. Tiefenbacher, R. Wetter, J. D. Koralek, A. Sarracini, K. Schnorr, C. Bostedt, A. Bodi, and A. A. Haddad, "Ultrathin liquid sheets: Water gets in shape for VUV absorption," Phys. Chem. Chem. Phys. **27**, 6457–6464 (2025).

[3] J. P. F. Nunes, K. Ledbetter, M. Lin, M. Kozina, D. P. DePonte, E. Biasin, M. Centurion, C. J. Crissman, M. Dunning, S. Guillet, K. Jobe, Y. Liu, M. Mo, X. Shen, R. Sublett, S. Weathersby, C. Yoneda, T. J. A. Wolf, J. Yang, A. A. Cordones, and X. J. Wang, "Liquid-phase mega-electron-volt ultrafast electron diffraction," Struct. Dyn. **7**, 024301 (2020).

[4] T. Gallo, L. Adriano, M. Heymann, A. Wrona, N. Walsh, G. Öhrwall, F. Callefo, S. Skruszewicz, M. Namboodiri, R. Marinho, J. Schulz, and J. Valerio,

"Development of a flat jet delivery system for soft X-ray spectroscopy at MAX IV," J. Synchrotron Radiat. **31**, 1285–1292 (2024).
[5]M. Vakili, J. Bielecki, J. Knoška, F. Otte, H. Han, M. Kloos, R. Schubert, E. Delmas, G. Mills, R. de Wijn, R. Letrun, S. Dold, R. Bean, A. Round, Y. Kim, F. A. Lima, K. Dörner, J. Valerio, M. Heymann, A. P. Mancuso, and J. Schulz, "3D printed devices and infrastructure for liquid sample delivery at the European XFEL," J. Synchrotron Radiat. **29**, 331–346 (2022).
[6]A. M. Gañán-Calvo, "Generation of steady liquid microthreads and micron-sized monodisperse sprays in gas streams," Phys. Rev. Lett. **80**, 285–288 (1998).
[7]D. P. DePonte, U. Weierstall, K. Schmidt, J. Warner, D. Starodub, J. C. H. Spence, and R. B. Doak, "Gas dynamic virtual nozzle for generation of microscopic droplet streams," J. Phys. D **41**, 195505 (2008).
[8]J. Eggers and E. Villermaux, "Physics of liquid jets," Rep. Prog. Phys. **71**, 036601 (2008).
[9]M. Kondoh and M. Tsubouchi, "Liquid-sheet jets for terahertz spectroscopy," Opt. Express **22**, 14135–14147 (2014).
[10]M. Ekimova, W. Quevedo, M. Faube, P. Wernet, and E. T. J. Nibbering, "A liquid flatjet system for solution phase soft-X-ray spectroscopy," Struct. Dyn. **2**, 054301 (2015).
[11]G. Galinis, J. Strucka, J. C. T. Barnard, A. Braun, R. A. Smith, and J. P. Marangos, "Micrometer-thickness liquid sheet jets flowing in vacuum," Rev. Sci. Instrum. **88**, 083117 (2017).
[12]J. C. T. Barnard, J. P. Lee, O. Alexander, S. Jarosch, D. Garratt, R. Picciuto, K. Kowalczyk, C. Ferchaud, A. Gregory, M. Matthews, and J. P. Marangos, "Delivery of stable ultra-thin liquid sheets in vacuum for biochemical spectroscopy," Front. Mol. Biosci. **9**, 1044610 (2022).
[13]A. Buchmann, C. Hoberg, and M. Havenith, "Improvements in windowless spectroscopy: 3D printed nozzles," in *47th International Conference on Infrared, Millimeter, and Terahertz Waves (IRMMW-THz)* (IEEE, 2022).
[14]Z. Yin, T. T. Luu, and H. J. Wörner, "Few-cycle high-harmonic generation in liquids: In-operando thickness measurement of flat microjets," J. Phys. Photonics **2**, 044007 (2020).
[15]D. J. Hoffman, T. B. van Driel, T. Kroll, C. J. Crissman, E. S. Ryland, K. J. Nelson, A. A. Cordones, J. D. Koralek, and D. P. DePonte, "Microfluidic liquid sheets as large-area targets for high repetition XFELs," Front. Mol. Biosci. **9**, 1048932 (2022).
[16]Y. P. Chang, Z. Yin, T. Balčiūnas, H. J. Wörner, and J. P. Wolf, "Temperature measurements of liquid flat jets in vacuum," Struct. Dyn. **9**, 014901 (2022).
[17]M. Fondell, S. Eckert, R. M. Jay, C. Weniger, W. Quevedo, J. Niskanen, B. Kennedy, F. Sorgenfrei, D. Schick, E. Giangrisostomi, R. Ovsyannikov, K. Adamczyk, N. Huse, P. Wernet, R. Mitzner, and A. Föhlisch, "Time-resolved soft X-ray absorption spectroscopy in transmission mode on liquids at MHz repetition rates," Struct. Dyn. **4**, 054902 (2017).
[18]K. M. George, J. T. Morrison, S. Feister, G. K. Ngirmang, J. R. Smith, A. J. Klim, J. Snyder, D. Austin, W. Erbsen, K. D. Frische, J. Nees, C. Orban, E. A. Chowdhury, and W. M. Roquemore, "High-repetition-rate (kHz) targets and optics from liquid microjets for high-intensity laser–plasma interactions," High Power Laser Sci. Eng. **7**, e50 (2019).
[19]T. T. Luu, Z. Yin, A. Jain, T. Gaumnitz, Y. Pertot, J. Ma, and H. J. Wörner, "Extreme–ultraviolet high–harmonic generation in liquids," Nat. Commun. **9**, 3723 (2018).
[20]A. D. Smith, T. Balčiūnas, Y.-P. Chang, C. Schmidt, K. Zinchenko, F. B. Nunes, E. Rossi, V. Svoboda, Z. Yin, J.-P. Wolf, and H. J. Wörner, "Femtosecond soft-x-ray absorption spectroscopy of liquids with a water-window high-harmonic source," J. Phys. Chem. Lett. **11**, 1981–1988 (2020).
[21]S. Menzi, G. Knopp, A. Al Haddad, S. Augustin, C. Borca, D. Gashi, T. Huthwelker, D. James, J. Jin, G. Pamfilidis, K. Schnorr, Z. Sun, R. Wetter, Q. Zhang, and C. Cirelli, "Generation and simple characterization of flat, liquid jets," Rev. Sci. Instrum. **91**, 105109 (2020).
[22]B. Ha, D. P. DePonte, and J. G. Santiago, "Device design and flow scaling for liquid sheet jets," Phys. Rev. Fluids **3**, 114202 (2018).
[23]C. J. Crissman, M. Mo, Z. Chen, J. Yang, D. A. Huyke, S. H. Glenzer, K. Ledbetter, J. P. F. Nunes, M. L. Ng, H. Wang, X. Shen, X. Wang, and D. P. DePonte, "Sub-micron thick liquid sheets produced by isotropically etched glass nozzles," Lab Chip **22**, 1365–1373 (2022).
[24]J. Yang, J. P. F. Nunes, K. Ledbetter, E. Biasin, M. Centurion, Z. Chen, A. A. Cordones, C. J. Crissman, D. P. DePonte, S. H. Glenzer, M.-F. Lin, M. Mo, C. D. Rankine, X. Shen, T. J. A. Wolf, and X. J. Wang, "Structure retrieval in liquid-phase electron scattering," Phys. Chem. Chem. Phys. **23**, 1308–1316 (2021).
[25]D. J. Hoffman, H. A. Bechtel, D. A. Huyke, J. G. Santiago, D. P. DePonte, and J. D. Koralek, "Liquid heterostructures: Generation of liquid–liquid interfaces in free-flowing liquid sheets," Langmuir **38**, 12822–12832 (2022).
[26]J. D. Koralek, J. B. Kim, P. Brůža, C. B. Curry, Z. Chen, H. A. Bechtel, A. A. Cordones, P. Sperling, S. Toleikis, J. F. Kern, S. P. Moeller, S. H. Glenzer, and D. P. DePonte, "Generation and characterization of ultrathin free-flowing liquid sheets," Nat. Commun. **9**, 1353 (2018).
[27]P. E. Konold, T. You, J. Bielecki, J. Valerio, M. Kloos, D. Westphal, A. Bellisario, T. Varma Yenupuri, A. Wollter, J. C. P. Koliyadu, F. H. M. Koua, R. Letrun, A. Round, T. Sato, P. Mészáros, L. Monroy, J. Mutisya, S. Bódizs, T. Larkiala, A. Nimmrich, R. Alvarez, P. Adams, R. Bean, T. Ekeberg, R. A. Kirian, A. V. Martin, S. Westenhoff, and F. R. N. C. Maia, "3D-printed sheet jet for stable megahertz liquid sample delivery at x-ray free-electron lasers," IUCrJ **10**, 662–670 (2023).
[28]F. Savart, "Mémoire sur le choc d'une veine liquide lancée contre un plan circulaire," Ann. Chim. **54**, 56–87 (1833).
[29]N. Dombrowski and R. P. Fraser, "A photographic investigation into the disintegration of liquid sheets," Philos. Trans. R. Soc. London, Ser. A **247**, 101–130 (1954).
[30]G. Taylor, "Formation of thin flat sheets of water," Proc. R. Soc. London, Ser. A **259**, 1–17 (1960).
[31]K. D. Miller, "Distribution of spray from impinging liquid jets," J. Appl. Phys. **31**, 1132–1133 (1960).
[32]D. S. Hasson and R. E. Peck, "Thickness distribution in a sheet formed by impinging jets," AIChE J. **10**, 752–754 (1964).
[33]E. A. Ibrahim and A. J. Przekwas, "Impinging jets atomization," Phys. Fluids A **3**, 2981–2987 (1991).
[34]J. D. Naber and R. D. Reitz, "Modeling engine spray/wall impingement," SAE Technical Paper No. 880107, 1988.
[35]R. Li and N. Ashgriz, "Characteristics of liquid sheets formed by two impinging jets," Phys. Fluids **18**, 087104 (2006).
[36]Lord Rayleigh, "On the capillary phenomena of jets," Proc. R. Soc. London **29**, 71–97 (1879).
[37]J. W. M. Bush and A. E. Hasha, "On the collision of laminar jets: Fluid chains and fishbones," J. Fluid Mech. **511**, 285–310 (2004).
[38]G. Belšak, S. Bajt, and B. Šarler, "Computational modeling and simulation of gas focused liquid micro-sheets," Int. J. Multiphase Flow **140**, 103666 (2021).
[39]B. Šarler, R. Zahoor, and S. Bajt, "Alternative geometric arrangements of the nozzle outlet orifice for liquid micro-jet focusing in gas dynamic virtual nozzles," Materials **14**, 1572 (2021).
[40]R. Zahoor, S. Bajt, and B. Šarler, "Influence of gas dynamic virtual nozzle geometry on micro-jet characteristics," Int. J. Multiphase Flow **104**, 152–165 (2018).
[41]K. Kovačič and B. Šarler, "The kinetic energy transfer analysis between the gas and the liquid in flow focusing of the micro-jet," J. Phys.: Conf. Ser. **2766**, 012075 (2024).
[42]R. Zahoor, S. Bajt, and B. Šarler, "A numerical investigation of micro-jet characteristics in different pressure environments," Int. J. Hydromechatronics **4**, 368–383 (2021).
[43]R. Zahoor, R. Regvar, S. Bajt, and B. Šarler, "A numerical study on the influence of liquid properties on gas-focused micro-jets," Prog. Comput. Fluid Dyn., Int. J. **20**, 71–83 (2020).
[44]R. Zahoor, J. Knoška, S. Bajt, and B. Šarler, "Experimental and numerical investigation of gas-focused liquid micro-jet velocity," Int. J. Multiphase Flow **135**, 103530 (2021).
[45]B. Zupan, R. Zahoor, S. Bajt, and B. Šarler, "Numerical treatment of electrical properties in two-phase electrohydrodynamic systems," Phys. Fluids **37**, 083353 (2025).
[46]R. Zahoor, G. Belšak, S. Bajt, and B. Šarler, "Simulation of liquid micro-jet in free expanding high-speed co-flowing gas streams," Microfluid. Nanofluid. **22**, 87 (2018).
[47]R. Zahoor, S. Bajt, and B. Šarler, "Numerical investigation on influence of focusing gas type on liquid micro-jet characteristics," Int. J. Hydromechatronics **1**, 222–237 (2018).

[48]V. Sanjay and A. K. Das, "Formation of liquid chain by collision of two laminar jets," Phys. Fluids **29**, 112102 (2017).
[49]S. P. Lin, Z. W. Lian, and B. J. Creighton, "Absolute and convective instability of a liquid sheet," J. Fluid Mech. **220**, 673–689 (1990).
[50]S. S. Ade, P. K. Kirar, L. D. Chandrala, and K. C. Sahu, "Droplet breakup and size distribution in an airstream: Effect of inertia," Phys. Rev. Fluids **9**, 084004 (2024).
[51]S. S. Ade, P. K. Kirar, L. D. Chandrala, and K. C. Sahu, "Droplet size distribution in a swirl airstream using in-line holography technique," J. Fluid Mech. **954**, A39 (2023).
[52]S. S. Ade, L. D. Chandrala, and K. C. Sahu, "Size distribution of a drop undergoing breakup at moderate Weber numbers," J. Fluid Mech. **959**, A38 (2023).
[53]J. Knoška, L. Adriano, S. Awel, K. R. Beyerlein, O. Yefanov, D. Oberthuer, G. E. Peña Murillo, N. Roth, I. Sarrou, P. Villanueva-Perez, M. O. Wiedorn, F. Wilde, S. Bajt, H. N. Chapman, and M. Heymann, "Ultracompact 3D microfluidics for time-resolved structural biology," Nat. Commun. **11**, 657 (2020).
[54]B. Zupan, G. E. Peña-Murillo, R. Zahoor, J. Gregorc, B. Šarler, J. Knoška, A. M. Gañán-Calvo, H. N. Chapman, and S. Bajt, "An experimental study of liquid micro-jets produced with a gas dynamic virtual nozzle under the influence of an electric field," Front. Mol. Biosci. **10**, 1006733 (2023).
[55]B. Zupan, S. Bajt, H. N. Chapman, and B. Šarler, "Acceleration of flow-focused liquid jets in the presence of a strong electric field," J. Phys.: Conf. Ser. **2766**, 012070 (2024).
[56]Nanoscribe GmbH, *User manual*, 2017, see https://www.Nanoscribe.de/En/.
[57]JCGM, *Evaluation of Measurement Data—Guide to the Expression of Uncertainty in Measurement* (ISO, Geneva, 2008).
[58]*ANSYS Fluent Theory Guide*, Ansys, Inc., Canonsburg, PA, 2021.
[59]T. K. Sengupta, A. Sengupta, N. Sharma, S. Sengupta, A. Bhole, and K. S. Shruti, "Roles of bulk viscosity on Rayleigh–Taylor instability," Phys. Fluids **28**, 094102 (2016).
[60]S. Chen, X. Wang, J. Wang, M. Wan, H. Li, and S. Chen, "Effects of bulk viscosity on compressible homogeneous turbulence," Phys. Fluids **31**, 085104 (2019).
[61]J. Lin, C. Scalo, and L. Hesselink, "Bulk viscosity model for near-equilibrium acoustic wave attenuation," arXiv:1707.05876 (2017).
[62]G. Buresti, "A note on Stokes' hypothesis," Acta Mech. **226**, 3555–3559 (2015).
[63]B. Sharma and R. Kumar, "Estimation of bulk viscosity of dilute gases using a nonequilibrium molecular dynamics approach," Phys. Rev. E **100**, 013309 (2019).
[64]X. Pan, M. N. Shneider, and R. B. Miles, "Coherent Rayleigh–Brillouin scattering in molecular gases," Phys. Rev. A **69**, 033814 (2004).
[65]S. Pan and E. Johnsen, "The role of bulk viscosity on the decay of compressible, homogeneous, isotropic turbulence," J. Fluid Mech. **833**, 717–744 (2017).
[66]R. Boukharfane, P. J. M. Ferrer, A. Mura, and V. Giovangigli, "On the role of bulk viscosity in compressible reactive shear layer developments," Eur. J. Mech.-B/Fluids **77**, 32–47 (2019).
[67]G. J. Prangsma, A. H. Alberga, and J. J. M. Beenakker, "Ultrasonic determination of the volume viscosity of N_2, CO, CH_4 and CD_4 between 77 and 300 K," Physica **64**, 278–288 (1973).
[68]G. Emanuel, "Bulk viscosity of a dilute polyatomic gas," Phys. Fluids A **2**, 2252–2254 (1990).
[69]L. Tisza, "Supersonic absorption and Stokes' viscosity relation," Phys. Rev. **61**, 531–536 (1942).
[70]Y. J. Kim, Y.-J. Kim, and J.-G. Han, "Numerical analysis of flow characteristics of an atmospheric plasma torch," arXiv:**0410237v1** (2004).
[71]K. Kovačič, S. Bajt, and B. Šarler, "Numerical analysis of Knudsen number of helium flow through gas-focused liquid sheet micro-nozzle," Fluids **9**, 273 (2024).
[72]P. J. Roache, "Quantification of uncertainty in computational fluid dynamics," Annu. Rev. Fluid Mech. **29**, 123–160 (1997).
[73]I. B. Celik, U. Ghia, P. J. Roache, C. J. Freitas, H. Coleman, and P. E. Raad, "Procedure for estimation and reporting of uncertainty due to discretization in CFD applications," J. Fluids Eng. **130**, 078001 (2008).